Nonlinear Dyn (2021) 105:131–166
https://doi.org/10.1007/s11071-021-06613-x

ORIGINAL PAPER

Nonlinear dynamic analysis of CNC lathe spindle-bearing system considering thermal effect

Haiyang Liu · Yimin Zhang · Changyou Li · Zhenyuan Li

Received: 13 January 2021 / Accepted: 8 June 2021 / Published online: 29 June 2021

Abstract The thermal effect has a significant influence on the performance of angular contact ball bearings and thus affects the motion accuracy and stability of spindle-bearing system of computerized numerical control (CNC) lathe. In this paper, a comprehensive coupled CNC lathe spindle-bearing model considering the thermal effect is proposed to predict the dynamic characteristics of system. The spindle is modeled as Timoshenko's beam by considering the centrifugal force and gyroscopic effects. The bearing is analyzed by a five degrees-of-freedom (DOF) quasi-static model considering the thermal effect in order to obtain the static deformations and thermal deformations of rolling bodies. The dynamic differential equation of system is established by the finite element method. Runge–Kutta integral method is used to solve the system equation numerically to study its nonlinear dynamic behaviors. The correctness of thermal model of CNC lathe spindle-bearing system is verified by testing the housing temperature. The simulation values of system response considering thermal effect or not are compared with the experimental results, which shows that the proposed model is feasible. Moreover, the effects of key parameters such as rotational speed, pulley eccentricity and bearing preload on the nonlinear characteristics of system are investigated. Single-periodic, multi-periodic, quasi-periodic and chaotic motions are observed by time history curve, 3-D frequency spectrum curve, phase diagram, Poincare section and bifurcation diagram under different operating conditions. The analytical model developed here can be also helpful to the design and optimization of CNC lathe spindle-bearing system.

Keywords Spindle-bearing system · Angular contact ball bearing · Quasi-static analysis · Bearing temperature distribution · Nonlinear vibration · Dynamic behaviors

1 Introduction

As the core component of CNC machine tools, spindle bearing system will generate a lot of heat when running at a high speed, which will have a great impact on the cutting stability and machining accuracy of CNC machine tools [1]. Therefore, it is very important to analyze and evaluate the dynamic characteristics of system for improving its machining accuracy and providing guidances to optimize its design. At present, the machining accuracy of CNC machine tools is

H. Liu · C. Li · Z. Li
School of Mechanical Engineering and Automation, Northeastern University, Shenyang 110819, China

Y. Zhang (✉)
Equipment Reliability Institute, Shenyang University of Chemical Technology, Shenyang 110142, China
e-mail: zhangyimin@syuct.edu.cn

required to be higher and higher [2]. The research on the thermal effect of bearings is a very complicated work [3], which involves the change of thermal resistance, bearing parameters, lubricant viscosity and the calculation of heat source, etc., because the dynamic characteristics of system are directly affected by bearing performance, especially the thermal effect of bearings [4, 5]. Therefore, the study of dynamic characteristics of CNC lathe spindle-bearing system should not only consider the mechanical characteristics of spindle, but also the thermal–mechanical coupling effect caused by the high-speed operation of bearings [6–8].

Angular contact ball bearings are most frequently used in machine tools due to their favorable stiffness properties, low friction loss and ability to bear axial and radial loads. With the increase of friction heat generated by bearings, the temperature distribution inside bearings will have a significant impact on their stiffness, working accuracy and even service life [9]. Over the years, many researchers have devoted themselves to the study of bearing heat transfer. Palmgren [10] was one of the early researchers who studied the mechanism of bearing temperature and put forward an empirical formula to calculate the friction torque. Subsequently, Harris and Kotzalas [11] proposed one of the most widely used comprehensive formula of bearing friction loss power on the basis of Palmgren's research. Later, Brecher et al. [12] proposed a new, simple calculation model to estimate the cage-induced frictional losses in spindle bearings under high rotational speed by experiments. Than et al. [13] present an inverse method to estimate time-varying heat sources in a high-speed spindle based on experimental temperatures of housing surface, because the thermal estimation accuracy of the empirical formula is relatively low. The frictional thermal mechanism of bearings was further studied by many scholars for more accurate assessments. Tong et al. [14] explored the running torque when the angular misalignment of angular contact ball bearings was factored. A skidding analysis of angular contact ball bearings subjected to various boundary conditions was implemented by Oktaviana et al. [15]. Zhang et al. [16] proposed a friction torque model of ball bearings with geometrical imperfections.

Combining the friction heat source and the nodes of spindle-bearing system, the heat balance equations can be established to solve the node temperatures by the thermal network method [17]. The thermal deformations of the balls and the inner and outer raceways can be obtained by the temperature distribution of bearing parts [18]. Lin and Tu [19] introduced the thermal deformations of rolling bodies into the study on thermal–mechanical coupling of bearings. Alfares et al. [20] investigated thermal variation impact on the dynamics of a spindle-bearing system by considering thermal deformation. However, the change of contact angle was not taken into account, so that the calculation of friction heat is inaccurate. Zheng et al. [21, 22] established a ball load balance model considering centrifugal force, gyroscopic torque and thermal deformation, where the change of contact angle was considered to improve the accuracy of calculation results. Subsequently, the effect of structure and assembly constraints on temperature of high-speed angular contact ball bearings with thermal network method was investigated by Zheng et al. [23]. Liu et al. [24] proposed the closed-loop iterative modeling method of thermal characteristics and analyzed the thermal–structure interaction mechanism to improve the modeling accuracy.

As the most complex and accurate theoretical model to describe the dynamic characteristics of spindle, Timoshenko beam model takes into account the moment of inertia and shear deformation [19, 25]. In recent years, many scholars have proposed a coupling model based on finite element spindle model and bearing model [26–28]. Li et al. [29] presented the dynamic model of high-speed motorized spindle in free state and working state. Xi et al. [30] proposed a new dynamic modeling method for a spindle-bearing system supported by angular contact ball bearings and floating displacement bearings to study the influence of key parameters on the system dynamics. The above model provides a theoretical basis for the study of rotor dynamics, but ignores the thermal effect of bearings. Li and Shin [31, 32] proposed a bearing load model including thermal deformation based on discrete spindle dynamic model, and then analyzed the bearing stiffness, thermal deformation and natural frequency of spindle system. Truong et al. [33] proposed a new workflow for analyzing the thermal–mechanical properties of a spindle-bearing system by adding the stiffness coefficient affected by temperature into the finite element model. Zheng et al. [34] studied the thermal estimation of angular contact ball bearings with vibration effects. Based on the error

mechanism of spindle system, Liu et al. [35] carried out thermal error modeling and compensation.

According to the above research, few studies take thermal effect into consideration in spindle-bearing system and carry out thorough research on its nonlinear characteristics, which is not conducive to the analysis of dynamic behaviors of system. The purpose of this work is to propose a comprehensive spindle-bearing system model of CNC lathe considering thermal effect to analyze the nonlinear characteristics of system. Firstly, a spindle model based on the Timoshenko's beam theory is established, and a five DOF quasi-static model of bearings considering thermal effect is proposed. The validity of spindle-bearing thermal model is verified by experiments at different speeds. Then, the comparison between numerical results and experimental results of system response shows that the proposed model is feasible. And then, the variation of contact angle, contact load and bearing stiffness with rotational speed and preload between balls and raceways are compared and analyzed under the condition of considering thermal effect or not. In order to investigate the effects of rotational speed, pulley eccentricity and bearing preload on the nonlinear characteristics of system, time history curve, frequency-spectrum curves, phase diagram, Poincare section and bifurcation diagram are employed. Finally, some conclusions are drawn to predict the motion accuracy and stability of system.

2 Dynamic model of spindle-bearing system

A lathe spindle refers to the shaft on the lathe that drives the workpiece to rotate. As shown in Fig. 1, a spindle component is usually composed of a shaft, a bearing, and a transmission element (pulley). It is mainly used to support transmission parts in machine tools to transmit motion and torque. The spindle contains two sets of angular contact ball bearings. The front two bearings are in tandem and three bearings are tandem at the rear. Preload is used for positioning and preload the inner raceway of bearings, which is conducive to obtaining higher bearing stiffness.

2.1 Dynamic equation of the spindle

According to the structure of spindle, it is discretized into a finite number of beam elements in Fig. 2. The specific spindle unit parameters can be found in Table 1. Timoshenko beam is used to model the beam elements, where each node has three translational degrees of freedom and two rotational degrees of freedom. Similar to the kinetic energy of pulley, the total kinetic energy of beam element includes horizontal motion energy and rotational kinetic energy. The total potential energy of beam element includes the elastic bending potential energy, shear potential energy and axial compression potential energy of beam.

According to the generalized Hamilton's Principle, the dynamic equation of the spindle obtained is rewritten into the matrix form by finite element method as follows:

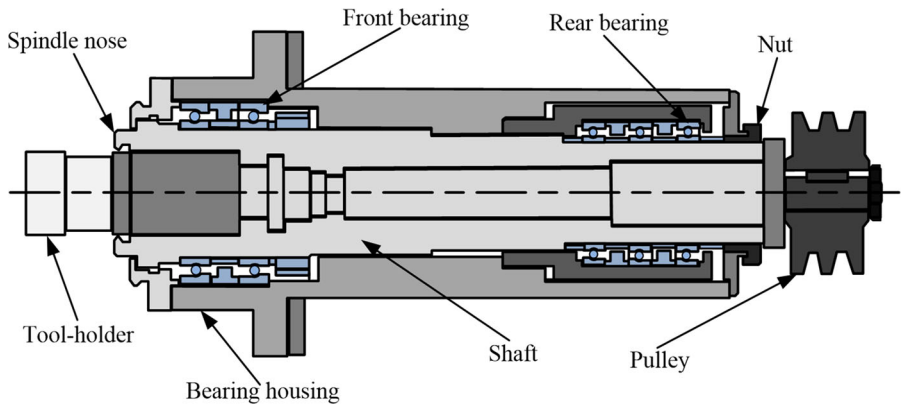

Fig. 1 A CNC spindle-bearing system

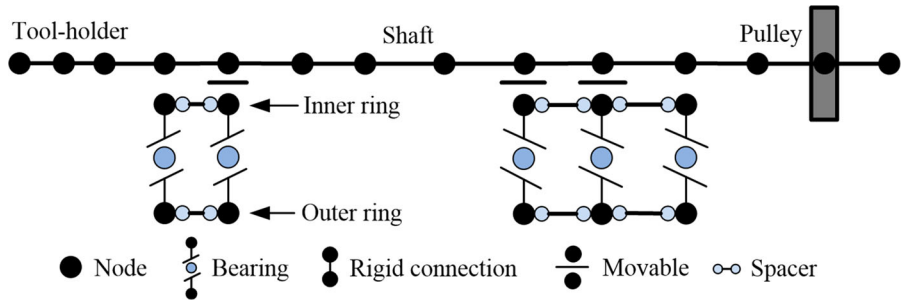

Fig. 2 Finite element node diagram of the machine tool spindle

Table 1 Dimensions of CNC lathe spindle unit

Unit number	Length (mm)	Inner/outer diameters(mm)	Unit number	Length (mm)	Inner/outer diameters(mm)	Unit number	Length (mm)	Inner/outer diameters(mm)
1	50	50/150	2	30	40/120	3	40	40/130
4	60	40/100	5	110	50/80	6	120	50/80
7	100	50/80	8	40	40/65	9	40	40/65
10	40	40/65	11	40	40/65	12	60	40/65
13	50	40/65						

$$(M^s + M^p)\ddot{q} - \Omega(G^s + G^p)\dot{q} + \left(K^s - \Omega^2 M_C^s\right)q = F^p \tag{1}$$

where M^s is the mass matrix of spindle, M^p represents the mass matrix of pulley, M_C^s is the mass matrix used for computing the centrifugal forces, G^s is the gyroscopic matrix of spindle, G^p represents the gyroscopic matrix of pulley, K^s is the stiffness matrix, and F^p represents unbalanced force. $q = \left(x, y, z, \varphi_y, \varphi_z\right)^T$ represents displacement vector. The details of matrices can be obtained by the finite element matrices [36].

2.2 Thermal model of spindle-bearing system

2.2.1 *Ball loads analysis of angular contact ball bearing*

In fact, the thermal effect of bearing parts will change the center position of rolling bodies. Thus, the contact deformation of ball-raceway changes accordingly. In this paper, the thermal effect of bearing parts is integrated into the normal contact forces Q_{ij} and Q_{oj} between the jth ball with the inner and outer raceways. The centrifugal force F_{cj} and gyroscopic moment M_{gj} of balls at any position ψ_j are considered. The load equilibrium equations of the jth ball can be as follows [11]:

$$\begin{cases} Q_{ij}\sin\alpha_{ij} - Q_{oj}\sin\alpha_{oj} - {M_{gj}}/{D_b}\left(\lambda_{ij}\cos\alpha_{ij} - \lambda_{oj}\cos\alpha_{oj}\right) = 0 \\ Q_{ij}\cos\alpha_{ij} - Q_{oj}\cos\alpha_{oj} + {M_{gj}}/{D_b}\left(\lambda_{ij}\sin\alpha_{ij} - \lambda_{oj}\sin\alpha_{oj}\right) + F_{cj} = 0 \end{cases} \tag{2}$$

where $\lambda_{ij} = 0$ and $\lambda_{oj} = 2$ represent the friction coefficients between the jth ball and the inner and outer raceways, respectively, which can be determined according to the outer raceway control theory [37]. α_{ij} and α_{oj} are the normal contact forces and contact angles between the jth ball with the inner and outer raceways, respectively.

The geometric constraint equations considering the thermal expansion of bearing parts shown in Fig. 3 can be expressed as [11]:

$$\begin{cases} \left(A_{1j} - Z_{1j}\right)^2 + \left(A_{2j} - Z_{2j}\right)^2 - \left((f_i - 0.5)D_b + \delta_{ij} - \varepsilon_b\right)^2 = 0 \\ Z_{1j}^2 + Z_{2j}^2 - \left((f_o - 0.5)D_b + \delta_{oj} - \varepsilon_b\right)^2 = 0 \end{cases} \tag{3}$$

where D_b is the ball diameter, ε_b represents the thermal expansion of ball.f_i and f_o denote the groove curvature coefficients of inner and outer raceways, respectively;Z_{1j}, Z_{2j}, A_{1j} and A_{2j} are the auxiliary variables to describe the position relationship between bearing

parts. A_{1j} and A_{2j} can be expressed as:
where δ_x, δ_y, δ_z, φ_y, φ_z denote the displacements of

$$\begin{cases} A_{1j} = BD_b \sin\alpha + u_x = BD_b \sin\alpha + \delta_x + R_i\varphi_z \cos\psi_j - R_i\varphi_y \sin\psi_j \\ A_{2j} = BD_b \cos\alpha + u_r = BD_b \cos\alpha + \delta_z \sin\psi_j + \delta_y \cos\psi_j + \varepsilon_{ir} + u_{\text{cent}} - \varepsilon_{or} \end{cases} \tag{4}$$

inner raceway;ε_{ir} and ε_{or} denote the thermal expansion of inner and outer raceways, respectively;R_i denotes the orbit radius of inner raceway groove curvature center [10]. The centrifugal expansion u_{cent} of inner raceway can be estimated as [22]:

$$u_{\text{cent}} = \frac{\rho\omega_c^2}{32E} d_m \left[D_i^2(3+\mu) + d_m^2(1-\mu)\right] \tag{5}$$

where D_i is the inner diameter of spindle; ω_c is the rotational speed of spindle;ρ, E and μ are the density, elastic moduli and Poisson ratio of material of spindle, respectively.

Taking inner raceway as analytic targets, the force equilibrium equations can be obtained as:

$$\begin{cases} F_x - \sum_{j=1}^{j=Z} \left(Q_{ij}\cos\alpha_{ij} + \frac{\lambda_{ij}M_{gj}}{D_b}\sin\alpha_{ij} \right) \cos\psi_j = 0 \\ F_y - \sum_{j=1}^{j=Z} \left(Q_{ij}\cos\alpha_{ij} + \frac{\lambda_{ij}M_{gj}}{D_b}\sin\alpha_{ij} \right) \sin\psi_j = 0 \\ F_z - \sum_{j=1}^{j=Z} \left(Q_{ij}\sin\alpha_{ij} - \frac{\lambda_{ij}M_{gj}}{D_b}\cos\alpha_{ij} \right) = 0 \\ M_x - \sum_{j=1}^{j=Z} \left[\left(Q_{ij}\sin\alpha_{ij} - \frac{\lambda_{ij}M_{ij}}{D_b}\cos\alpha_{ij} \right) R_i + \frac{\lambda_{ij}M_{gj}}{D_b} f_i \right] \sin\psi_j = 0 \\ M_y - \sum_{j=1}^{j=Z} \left[\left(Q_{ij}\sin\alpha_{ij} - \frac{\lambda_{ij}M_{ij}}{D_b}\cos\alpha_{ij} \right) R_i + \frac{\lambda_{ij}M_{gj}}{D_b} f_i \right] \cos\psi_j = 0 \end{cases} \tag{6}$$

where F_x, F_y, F_z, M_x and M_y represent the external forces and moments acted on the inner raceway of bearing.Z indicates the number of balls.

The initial values of main variables δ_x, δ_y, δ_z, φ_x, φ_y are set, and the Newton–Rapshon method is used to solve the Eqs. (2) and (3) to obtain the auxiliary variables X_{1j}, X_{2j}, δ_{ij} and δ_{oj}. The obtained auxiliary variables are brought into Eq. (6) to verify whether the main variables meet the accuracy requirement. If the requirement is not met, the main variables are updated and returned to the previous step. The iteration will be terminated until the main variables meet the accuracy requirement. Finally, the contact forces Q_{ij}, Q_{oj} and contact angles α_{ij}, α_{oj} can be obtained.

2.2.2 Heat generation model

The friction torque [10] of rolling bearing is composed of two parts as shown in Eq. (7)

$$M = M_v + M_1 \tag{7}$$

where M_v is frictional torque generated by the viscous friction of lubricant and M_1 is frictional torque caused by applied load, which can be obtained according to reference [11].

The friction torque is distributed to the contact surfaces of balls with the inner and outer raceways [10]. The resulting power loss between the balls and the inner and outer raceways can be expressed as:

$$\begin{cases} P_{ij} = \omega_{mj} D_b / (Zd_i) M \\ P_{oj} = \omega_{mj} D_b / (ZD_o) M \end{cases} \tag{8}$$

where ω_{mj} is revolution speed of balls.

The spin-induced friction torques M_{sj} between the balls and the inner raceway can be rewritten as:

$$\begin{cases} M_{sj} = \dfrac{3\mu_{si} Q_{ij} \sum_j}{8} \\ P_{sj} = \omega_{sj} M_{sj} \end{cases} \tag{9}$$

where μ_{si} is the friction coefficient between the balls and inner raceway,ω_{sj} is the spin speed of balls and Σ_j is the second kind of complete contact elliptic integral between the balls and the raceways.

Combined with the above factors, the power loss of bearing, namely the total friction heat generated by the heat source, can be expressed as:

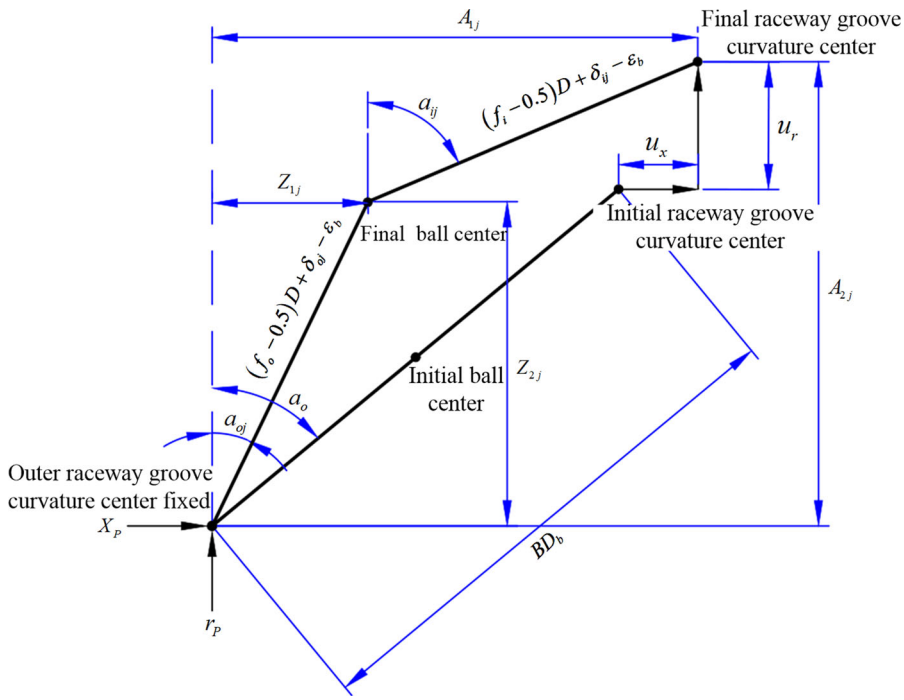

Fig. 3 Deformation relationship between ball and inner and outer raceways

$$P_{\text{total}} = P_i + P_o = \sum_{j=1}^{Z}\left(P_{ij} + P_{sj}\right) + \sum_{j=1}^{Z} P_{oj} \tag{10}$$

2.2.3 *Transient thermal network model*

Based on the principle of heat flux conservation, the general form of transient heat balance equation can be established as:

$$\begin{aligned}&\frac{T_0^{k+1}-T_1^{k+1}}{R_{0-1}}+\frac{T_0^{k+1}-T_2^{k+1}}{R_{0-2}}+\frac{T_0^{k+1}-T_3^{k+1}}{R_{0-3}}\\&+\frac{T_0^{k+1}-T_4^{k+1}}{R_{0-4}}\\&=Q_0-C_0\rho_0V_0\frac{T_0^{k+1}-T_0^{k}}{\Delta t_k}\end{aligned} \tag{11}$$

where T_0^{k+1} is the heat source temperature at t_{k+1}; T_0^k is the heat source temperature at t_k; T_i^{k+1} is the outside node temperature at t_{k+1}; $R_{0\text{-i}}$ is the thermal resistance between the heat source and the outside node (i = 1,2,3,4);Q_0 is the total frictional heat generated by the heat source;$\Delta t_k = t_{k+1} - t_k$ is the step size of time series.

Figure 4 shows the cross section of thermal network diagram of spindle-bearing element, which is divided into 9 nodes in this study. Therefore, we can obtain 9 equations similar to Eq. (11) to solve the temperature field of spindle-bearing system.

All nodes in Fig. 4 include three types of thermal resistance: conduction thermal resistance, contact thermal resistance and convection thermal resistance. The specific expressions of each thermal resistance are shown in Tables 2, 3 and 4.

Based on the above analysis, the process of solving the transient temperature field of spindle- bearing system by thermal network method can be obtained as shown in Fig. 5. The front and rear bearing sets adopt 7016C and 7014C, respectively. More detailed spindle-bearing system parameters are shown in Table 5. Firstly, given the spindle speed and system loading conditions, the ball loads equilibrium equations of bearings are established according to Sect. 2.2.1 to obtain the contact angle and contact load of balls. Then, the friction heat generated by bearings is calculated according to Sect. 2.2.2. At the same time, combining bearing parameters and taking room temperature as the initial temperature, the heat transfer coefficient of system components can be obtained according to the formulas in Tables 2, 3 and 4. Subsequently, the transient heat balance equations of system are established and solved based on Sect. 2.2.3. In the process of iterative solution, we

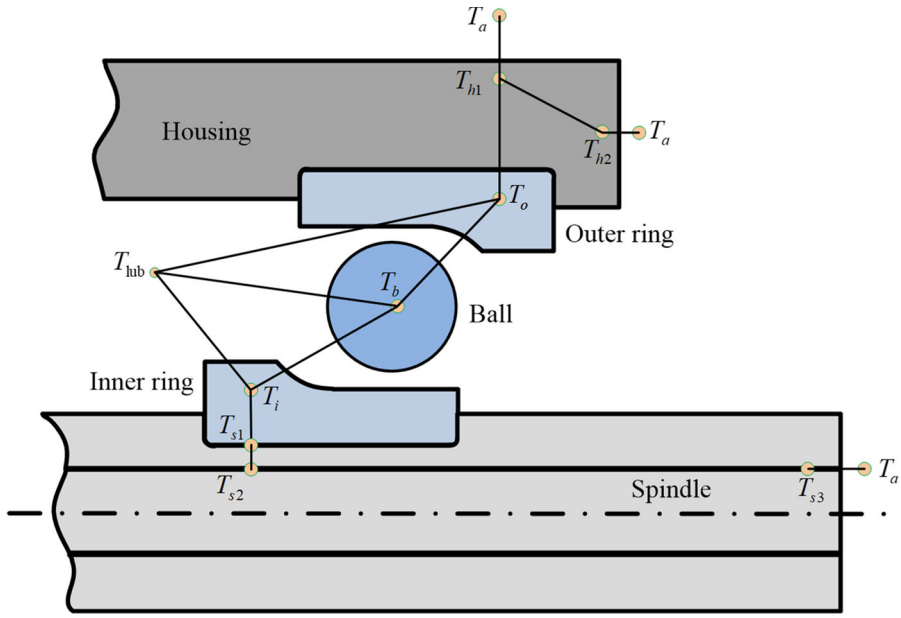

Fig. 4 Spindle unit thermal network node diagram

Table 2 Formula of thermal conduction resistance

Formula	Application situation	Reference
$R = \ln(d_{ext}/d_{\text{int}})/2\pi k_D L$	Inner/outer rings, housing and shaft	Ref. [38]
$R = \Delta L/AK$	Ball, shaft and housing	Ref. [39]

Table 3 Contact thermal resistance formula

Formula	Application situation	Reference
$R = \frac{1}{\pi}\left(\frac{a}{b}\right)\frac{1}{k_D a\sqrt{Pe}}$	Hertzian contact between balls and raceways	Ref. [38]
0.02; 0.1	Inner ring and shaft; outer ring and housing	Ref. [39, 40]

only need to solve the corresponding linear equations. If the temperature value obtained at this time does not converge, then the bearing parameters, lubricant viscosity and heat transfer coefficient are updated according to this temperature value and taken as the inputs for the next iteration calculation. The calculation does not stop until the results of temperature field meet the given convergence condition. Finally, the temperature values of key nodes of system are output to calculate the deformations of the rolling bodies.

Subsequently, ε_b and ε_{in} are the thermal expansion of balls and inner raceway can be calculated from Stein and Tu [46].ε_{out} is the thermal expansion of housing, which can be obtained as [47].

Hence, the total deformation δ_{ijt} of bearings caused by thermal effect can be expressed as:

$$\delta_{ijt} = \varepsilon_b + \frac{(\varepsilon_{\text{in}} - \varepsilon_{\text{out}})}{2} \tag{12}$$

2.2.4 *Calculation of stiffness matrix of angular contact ball bearing*

Under the condition of high-speed rotation of angular contact ball bearing, the balls are under the combined

Table 4 Convection thermal resistance formula

Formula	Application situation	Reference
$R = \frac{1}{A_w}\left(\frac{L}{k_D Nu}\right)$		Ref. [41]
$Nu = \left(1.2 + 0.53(\rho_{\text{lub}} D_b/\eta_{\text{lub}} \cdot \omega_m d_m/2)^{0.64}\right) \cdot (\eta_{\text{lub}}/\alpha_d \rho_{\text{lub}})^{0.3}\left(\eta_{T_b}/\eta_{T_{\text{lub}}}\right)$	Ball and lubricant	Ref. [42]
$\begin{cases} Nu = 2 & Ta < 41 \\ Nu = 0.167\left(\rho g_r (r_{in}\omega)\mu^{-1}\sqrt{g_r/r_{in}}\right)^{0.69}\text{Pr}^{0.4} & 41 < Ta < 100 \\ Nu = 0.401\left(\rho g_r (r_{in}\omega)\mu^{-1}\sqrt{g_r/r_{in}}\right)^{0.5}\text{Pr}^{0.4} & Ta > 100 \end{cases}$	Outer surface of inner ring and lubricant	Ref. [43]
$\begin{cases} Nu = 0.4\sqrt{\text{Re}}\,\text{Pr}^{1/3} & \text{Re} < 2.5 * 10^5 \\ Nu = 0.238\text{Re}^{0.8}\,\text{Pr}^{0.6} & \text{Re} > 3.2 * 10^5 \end{cases}$	Shaft end	Ref. [44]
$Nu = 0.825 + \frac{0.387\text{Re}^{1/6}}{\left(1+(0.492/\text{Pr})^{9/16}\right)^{8/27}}$	Housing end face and ambient air	Ref. [45]

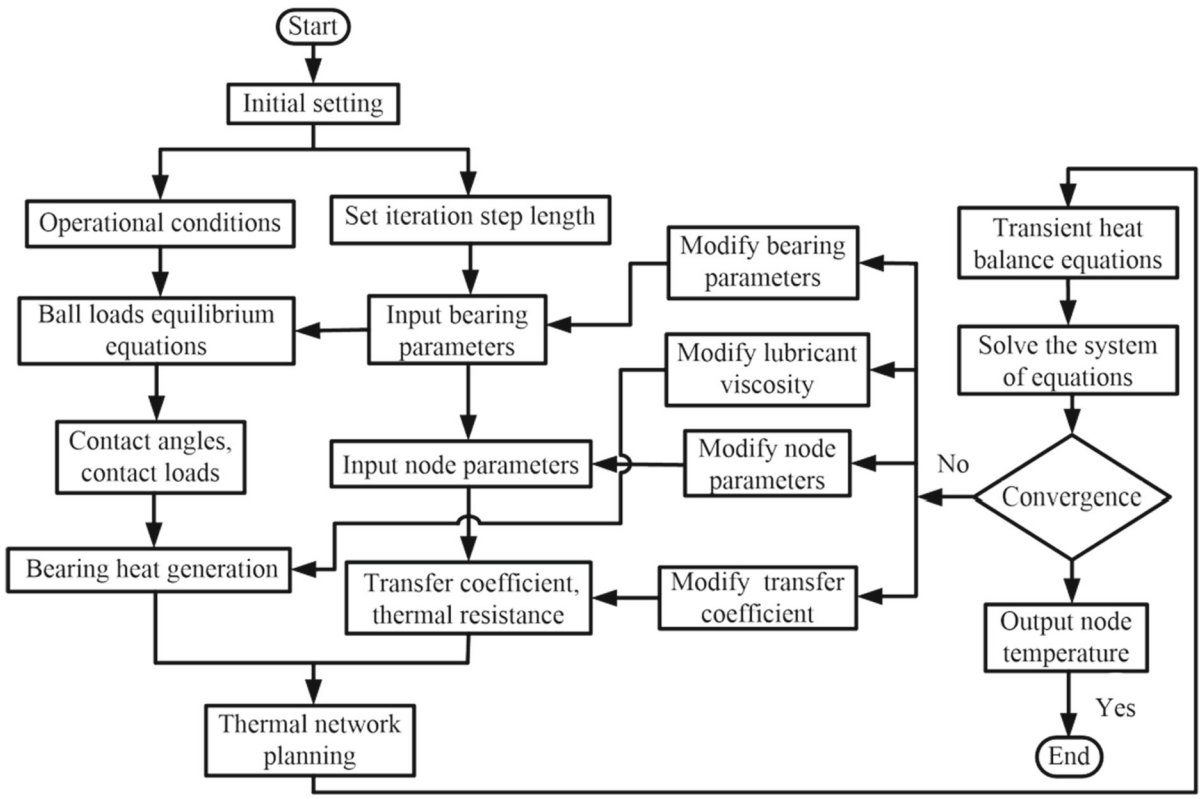

Fig. 5 Solution flow of transient temperature field of spindle-bearing system

action of centrifugal force, gyroscopic moment and the thermally-induced preload. According to the relationship between bearing parts deformation and acting force, it can be expressed as [31]:

$$K^b = -\frac{\partial F}{\partial \delta^T} = -\sum_{j=1}^{Z} [R]^T \frac{\partial Q_j^T}{\partial u_j}[R] \tag{13}$$

where

Table 5 Specifications of spindle-bearing system

Parameter	Value	Parameter	Value
Spindle density	$7.86*10^3$ kg/m^3	Poisson's ratio of ball	0.26
Specific heat capacity of spindle	485 J/(kg·°C)	Density of rings	$7.81*10^3$ kg/m^3
Spindle thermal conductivity	42.3 W/(m·°C)	Elasticity modulus of rings	207GPa
Bearing chamber density	$7.3*10^3$ kg/m^3	Poisson's ratio of rings	0.3
Specific heat capacity of bearing chamber	510 J/(kg·°C)	Specific heat capacity of rings	450 J/(kg·°C)
Bearing chamber thermal conductivity	45.0 W/(m·°C)	Rings thermal conductivity	40.1 W/(m·°C)
Ball density	$7.85*10^3$ kg/m^3	Relative radius of curvature	0.523
Specific heat capacity of ball	800 J/(kg·°C)	Bearing inner diameter	65 mm
Ball chamber thermal conductivity	11.6 W/(m·°C)	Bearing outer diameter	100 mm
Elasticity modulus of ball	320GPa	Number of balls	19
Initial contact angle	15°	Ball diameter	11.5 mm

$$\frac{\partial Q_j^T}{\partial u_j} = \begin{bmatrix} J_o J_b^{-1} J_i & 0 & 0 \\ 0 & 0 & 0 \\ 0 & 0 & 0 \end{bmatrix} \tag{14}$$

$$R = \begin{bmatrix} \cos(\psi_j) & \sin(\psi_j) & 0 & -R_p \sin(\psi_j) & R_p \cos(\psi_j) \\ 0 & 0 & 1 & R_i \sin(\psi_j) & -R_i \cos(\psi_j) \\ 0 & 0 & 0 & -\sin(\psi_j) & \cos(\psi_j) \end{bmatrix} \tag{15}$$

where R_p is the axial distance between the center of ball and the center of bearing inner raceway, J_b can be obtained by deriving the load balance Eq. (2) of balls in horizontal and vertical directions. $J_b = J_i + J_o$ is the obtained stiffness matrix.

2.2.5 *Nonlinear restoring forces and moments associated with the bearings*

The influence of thermal expansion of bearing parts on bearing performance is vital. Therefore, it is very necessary to consider the thermal effect of bearings to analyze the nonlinear dynamic characteristics of CNC lathe spindle-bearing system. The schematic diagram of system is shown in Fig. 6. Since the two sets of bearings are mounted back to back, the left bearing coordinate is consistent with the system coordinate, while the right bearing is opposite. Hence, the nonlinear restoring forces and moments of two sets of bearings should be derived respectively.

Ignoring the eccentricity of spindle, the dynamic displacements of spindle will only lead to the changes of deformation between balls and inner raceway. The dynamic deformation of the jth ball in the left bearing could be approximately expressed as [48]:

$$\delta_{ijdL} = \begin{bmatrix} -z \sin(\psi_j) \cos(\alpha_{ij}) + y \cos(\psi_j) \cos(\alpha_{ij}) + \\ \left(x + \varphi_z R_i \cos(\psi_j) - \varphi_y R_i \sin(\psi_j)\right) \sin(\alpha_{ij}) \end{bmatrix} \tag{16}$$

where $x, y, z, \varphi_y, \varphi_z$ denote the dynamic displacements of bearing inner raceway.δ_{ijtL} is the thermal deformation, which can be derived from Eq. (12). Then, the total deformation of the jth ball of left bearing could be expressed as:

$$\begin{aligned} \delta_{TL} &= \delta_{ijdL} + \delta_{ijsL} + \delta_{ijtL} \\ &= \delta_{ijdL} + \delta_{ijsL} + \varepsilon_b^L + \frac{\left(\varepsilon_{in}^L - \varepsilon_{out}^L\right)}{2} \end{aligned} \tag{17}$$

where δ_{ijsL} means the dynamic deformation and static deformation between the jth ball and inner raceway.

The nonlinear restoring forces and moments of the jth ball of left bearing in the global coordinate system could be determined as:

$$\begin{cases} F_{Lx} = -K\delta_{TL}^{1.5} \sin(\alpha_{ij}) \\ F_{Ly} = -K\delta_{TL}^{1.5} \cos(\alpha_{ij}) \cos(\psi_j) \\ F_{Lz} = K\delta_{TL}^{1.5} \cos(\alpha_{ij}) \sin(\psi_j) \\ M_{Ly} = K\delta_{TL}^{1.5} \sin(\alpha_{ij}) R_i \sin(\psi_j) \\ M_{Lz} = -K\delta_{TL}^{1.5} \sin(\alpha_{ij}) R_i \cos(\psi_j) \end{cases} \tag{18}$$

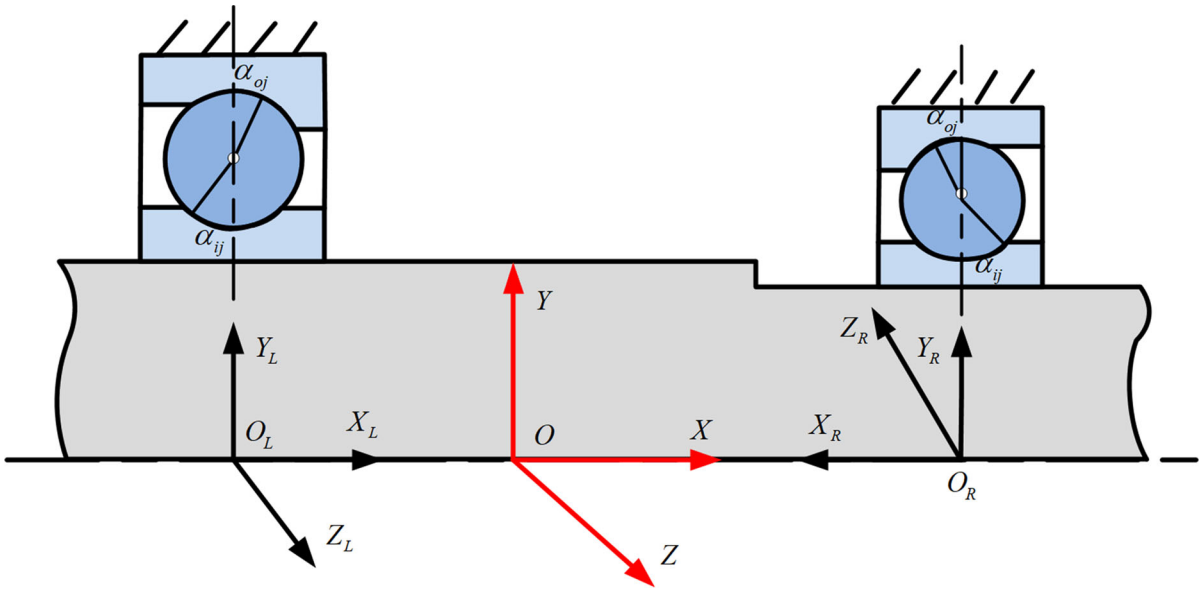

Fig. 6 Geometric relationship of spindle-bearing system

where K is the load–deflection parameter between the jth ball and the inner and outer raceways [11].

Similarly, the nonlinear restoring forces and moments of the jth ball of right bearing in the global coordinate system could be expressed as:

$$\begin{cases} F_{Rx} = K\delta_{TR}^{1.5}\sin(\alpha_{ij}) \\ F_{Ry} = -K\delta_{TR}^{1.5}\cos(\alpha_{ij})\cos(\psi_j) \\ F_{Rz} = -K\delta_{TR}^{1.5}\cos(\alpha_{ij})\sin(\psi_j) \\ M_{Ry} = K\delta_{TR}^{1.5}\sin(\alpha_{ij})R_i\sin(\psi_j) \\ M_{Rz} = K\delta_{TR}^{1.5}\sin(\alpha_{ij})R_i\cos(\psi_j) \end{cases} \tag{19}$$

By assembling equations of spindle and bearings, the nonlinear dynamic equations for CNC lathe spindle-bearing system can be obtained:

$$M\ddot{q} + C\dot{q} + Kq = F(t) \tag{20}$$

where
$M = M^s + M^p$,$C = G^s + G^p + C^s$,-
,$K = K^s - \Omega^2 M_C^s$,$F^b(q)$ is the vector of nonlinear restoring force and moments associated with bearings from Eqs. (18) and (19). Among them,$C^s = \alpha M + \beta K$ is the structural damping which can be expressed as [49]:

$$\begin{cases} \alpha = 2\left(\dfrac{\xi_2}{\omega_2} - \dfrac{\xi_1}{\omega_1}\right)\Big/\left(\dfrac{1}{\omega_2^2} - \dfrac{1}{\omega_1^2}\right) \\ \beta = 2(\xi_2\omega_2 - \xi_1\omega_1)/(\omega_2^2 - \omega_1^2) \end{cases} \tag{21}$$

where ω_1 and ω_2 are the first two natural frequencies of CNC lathe spindle-bearing system, respectively.ξ_1 and ξ_2 are the corresponding damping ratios, respectively.

By using the restoring force method, the total nonlinear restoring forces and moments of bearings are added into the force vector of system. The specific parameters of CNC lathe spindle-bearing system can be obtained from the Tables 1 and 5 in this paper. Thus, the mathematical expression of system differential equation can be obtained. For this purpose, the ODE45 function (an explicit Rung-Kutta method) is used to solve Eq. (20) through MATLAB software.

3 Experimental validation

The experiment rig of CNC lathe spindle-bearing system shown in Fig. 7 is used to verify the feasibility of proposed model. The specific parameters of CNC lathe spindle-bearing system are listed in Tables 1 and 5. The schematic diagram of system experimental device is shown in Fig. 8. The rear bearing (NSK 7013C) of system is taken as the experimental object

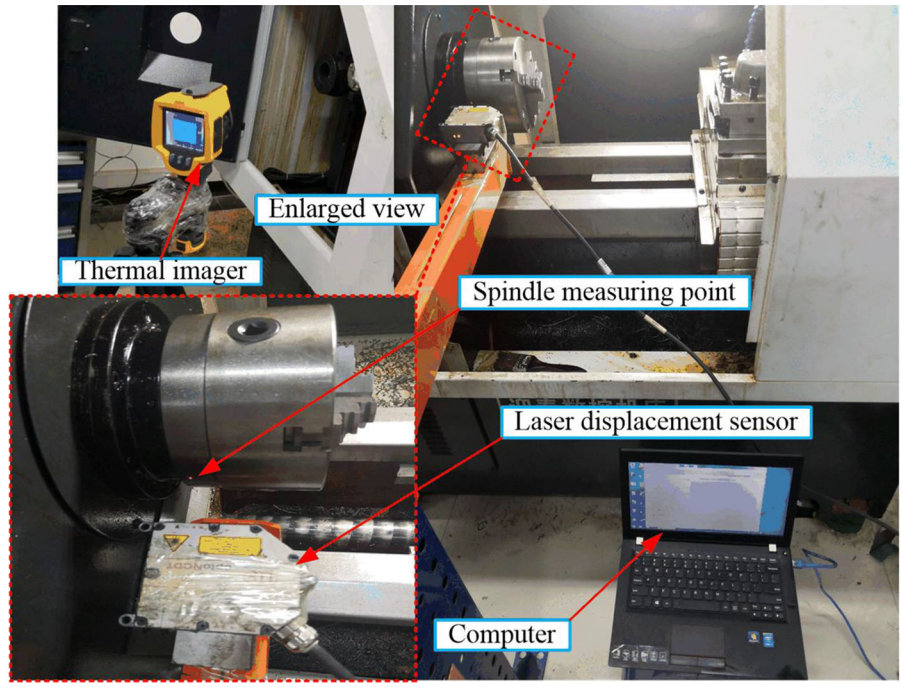

Fig. 7 Radial response experiment rig for CNC lathe spindle-bearing system

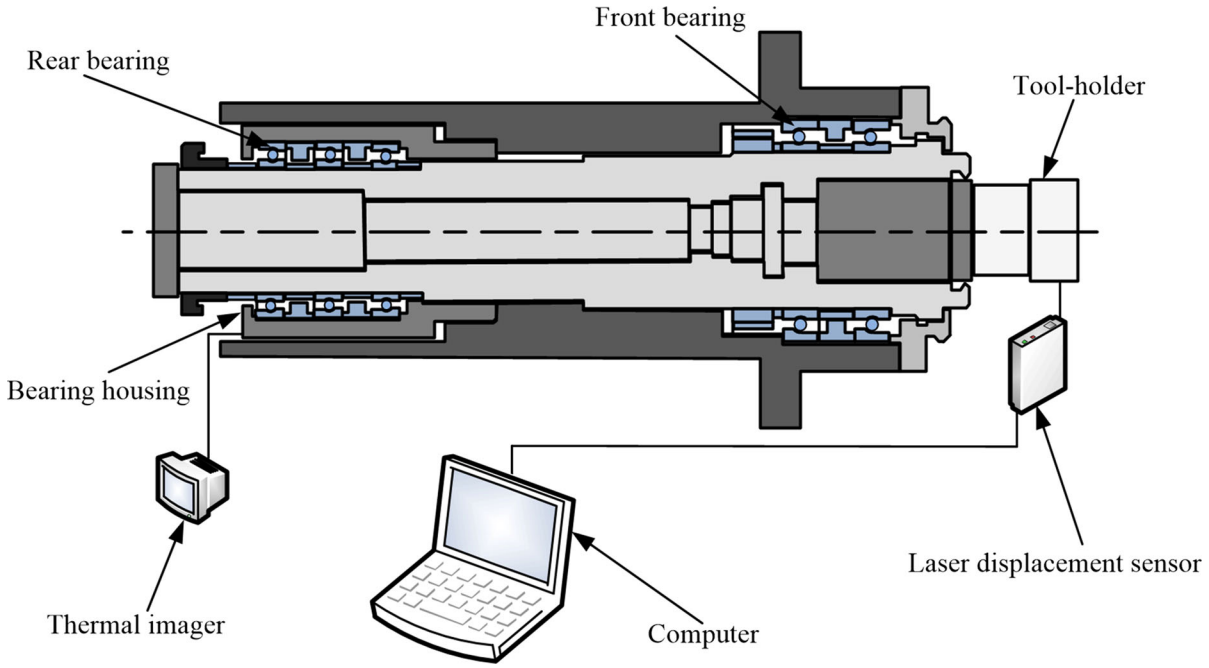

Fig. 8 Schematic diagram of CNC lathe spindle-bearing system experiment rig

in this study. The infrared thermal imager (model: FLUKE Ti32) is used to monitor the temperature of housing at the tail of spindle. All tests are carried out in a laboratory with a controlled ambient temperature of 24–26 °C and a relative humidity of 20–25%.

The spindle-bearing system is frequency swept by using an experimental device as shown in Fig. 7. The rotational speed of spindle starts from 0 r/min, and the rotational speed increment is 100 r/min and increases to 3000 r/min. The radial displacement data of spindle end are measured by using laser displacement sensor (model: optoNCDT2300-20) and LabView software in the computer. Fast Fourier Transform is carried out on the radial responses at each rotating speed to obtain their corresponding amplitudes, and all amplitudes are fitted to obtain the frequency response curve as shown in Fig. 9. Where ω_{a1} = 250 r/min, ω_{b1} = 318 r/min, ω_{n1} = 280 r/min and ω_{a2} = 530 r/min, ω_{b2} = 600 r/min, ω_{n2} = 560 r/min. The damping ratio is estimated by using the half power bandwidth method, which can be expressed as [50]:

$$\xi_i = (\omega_{bi} - \omega_{ai})/\omega_{ni} \tag{22}$$

The first two damping ratios of CNC lathe spindle-bearing system are ξ_1 = 0. 1214 and ξ_2 = 0. 0625, respectively.

As shown in Fig. 10, the trend of the theoretical values is the same as the experimental results. The deviation between theoretical values and experiment results is small and the coincidence degree is high, which proves that the thermal model adopted is reasonable for the thermal calculation of CNC lathe spindle-bearing system. With the spindle operating, the laser displacement sensor (model: optoNCDT2300-20) collects the radial response of spindle to be tested in real time.

Figure 11 depicts the comparison of simulation values and experimental results for the variation of spindle radial response with operation time at three different rotational speeds of 1500 r/min, 2000 r/min and 2500 r/min. With the increase of rotational speed, the radial response of spindle gradually increases and tends to be stable. Compared with the simulation values without thermal effect, the experimental results are closer to the simulation values with thermal effect, which proves the correctness of proposed model in this study.

4 Results and discussion

4.1 The influence of rotational speed and preload on contact angle and contact load

Figure 12 shows the variation of contact angle and contact load with rotational speed when the bearing preload is 500 N with or without thermal deformation. The contact angle and contact load considering thermal deformation are smaller than those without

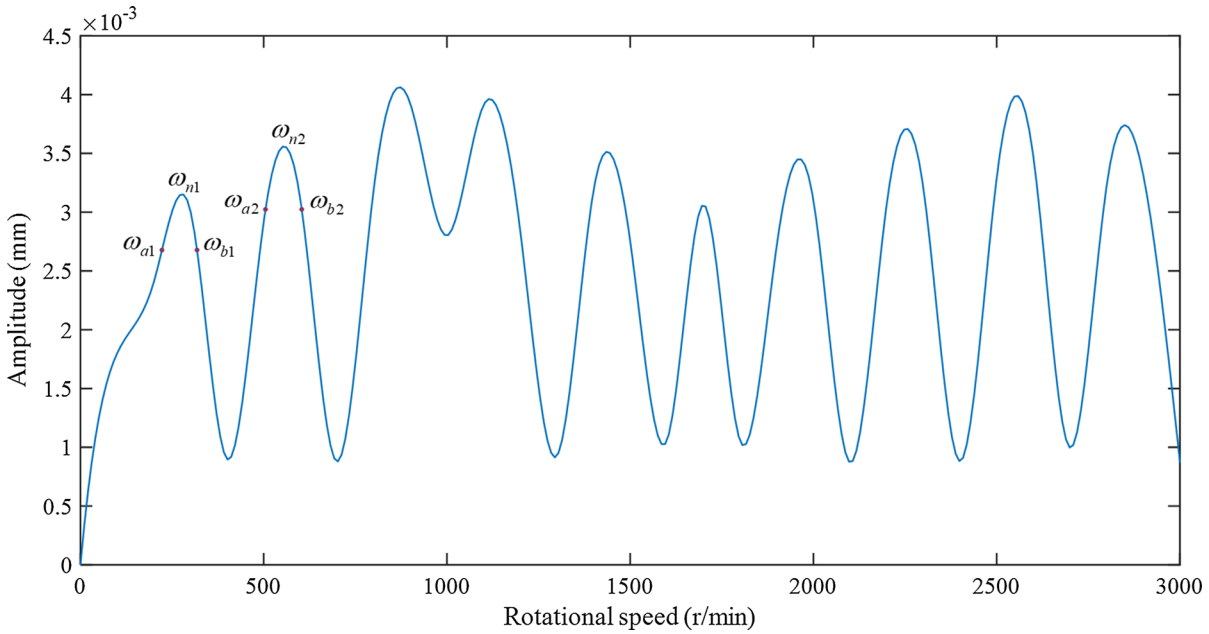

Fig. 9 Frequency response experimental curve of CNC lathe spindle

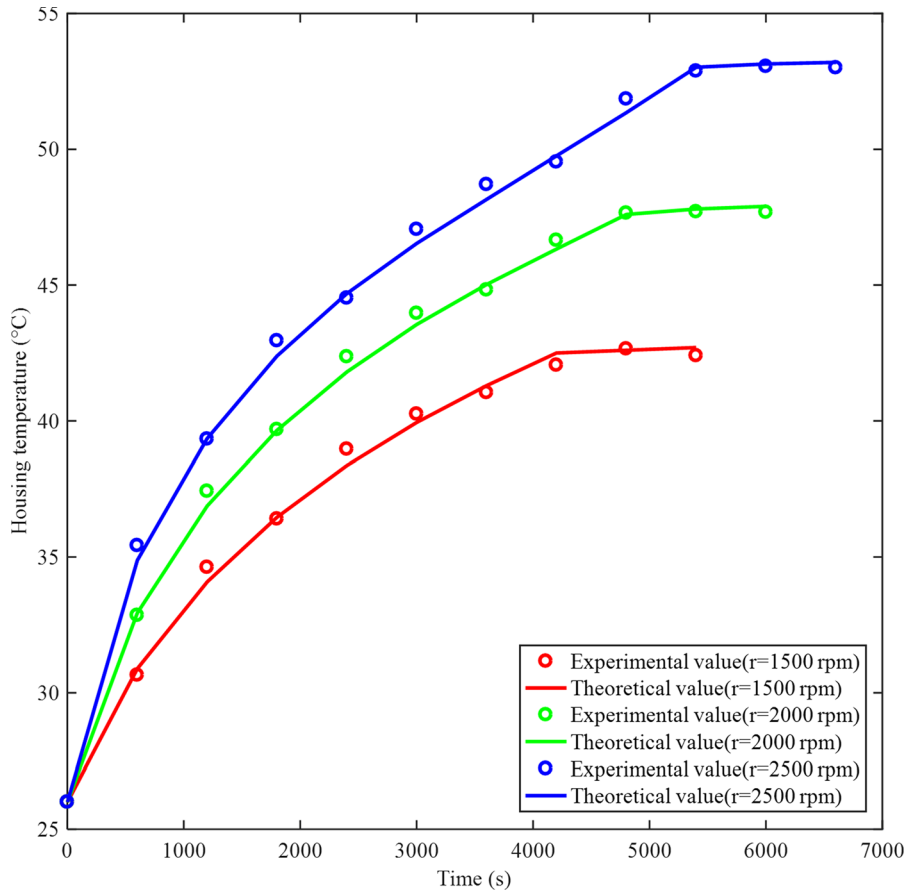

Fig. 10 Comparison of theoretical and experimental results of housing temperature

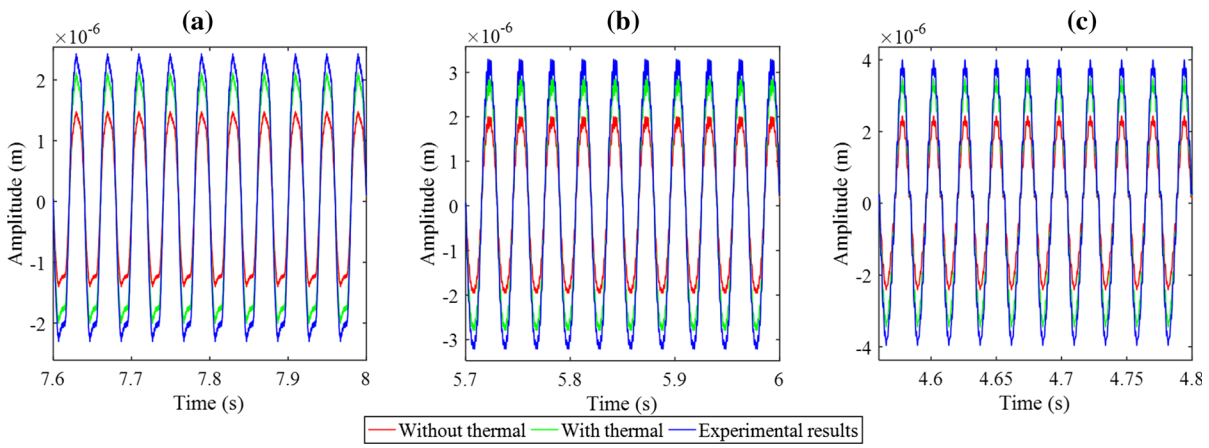

Fig. 11 Comparison of simulation and experiment results of radial response of CNC lathe spindle-bearing system: **a** 1500 r/min; **b** 2000 r/min; **c** 2500 r/min

thermal deformation. Because the thermal deformation of bearing parts makes the radial distance between the curvature centers of inner and outer raceways of bearing large, this causes a decrease in the contact angle. Meanwhile, due to the temperature rise of bearing parts is uneven and the size of outer raceway is larger than that of inner raceway, which lead to a negative total thermal deformation, resulting in a

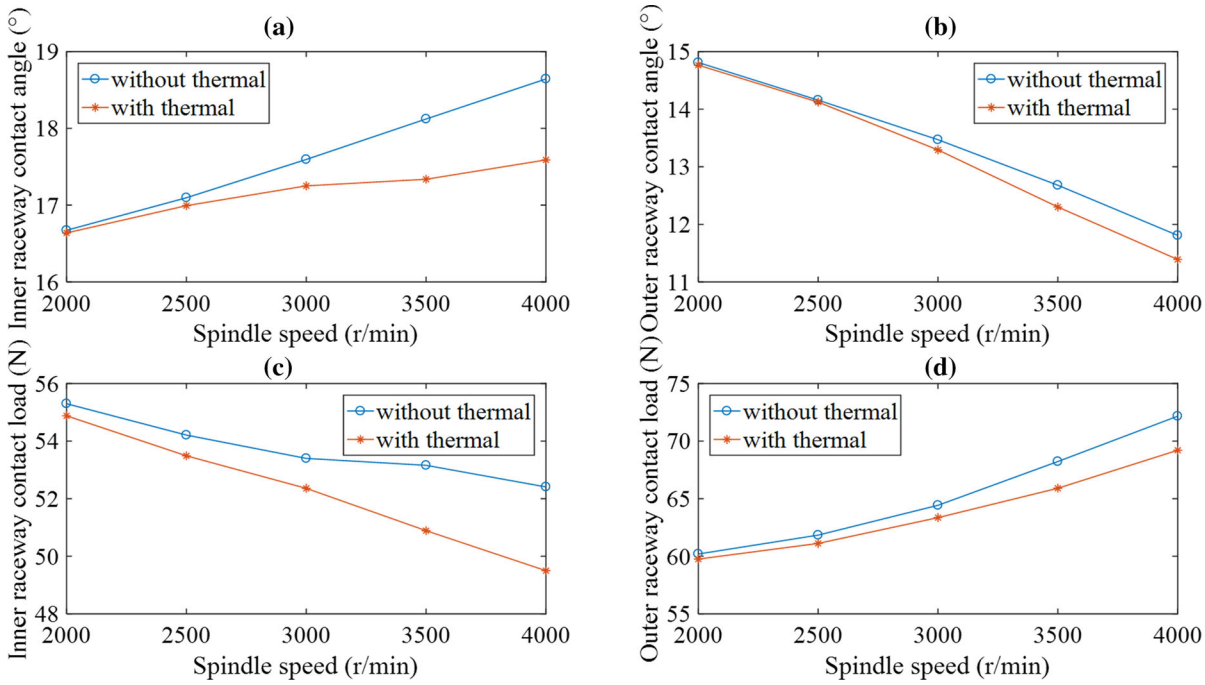

Fig. 12 Relationship between spindle speed and contact angle and contact load of bearing

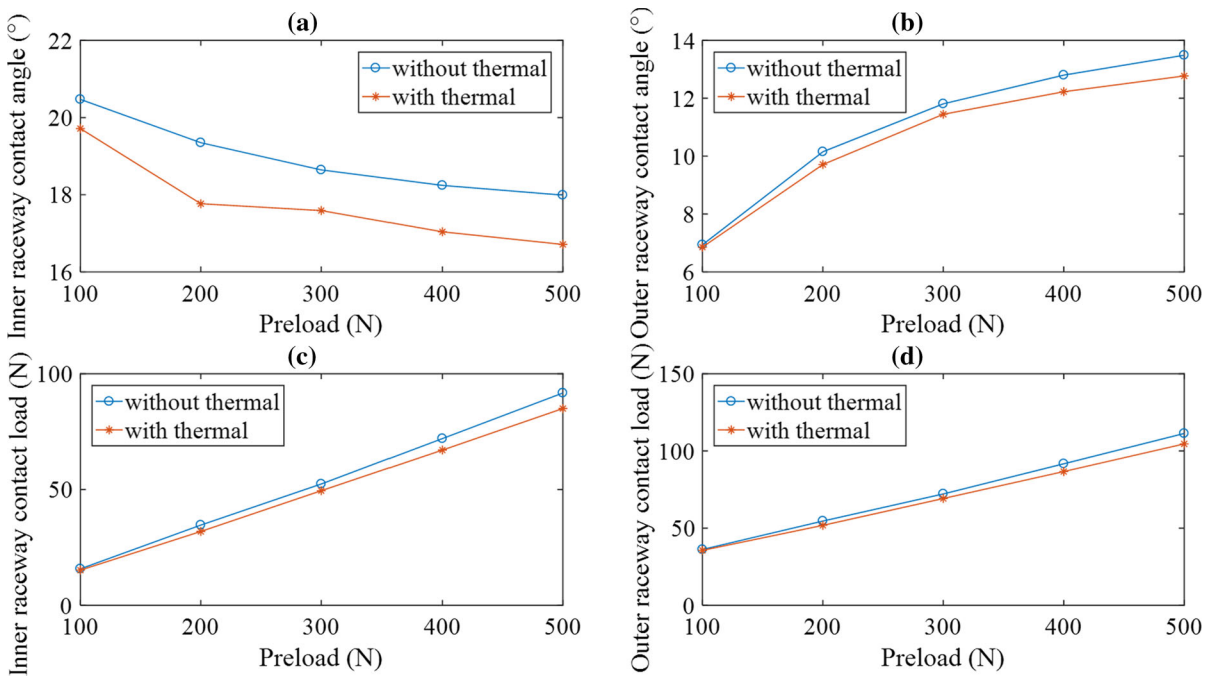

Fig. 13 Relationship between preload and contact angle and contact load of bearing

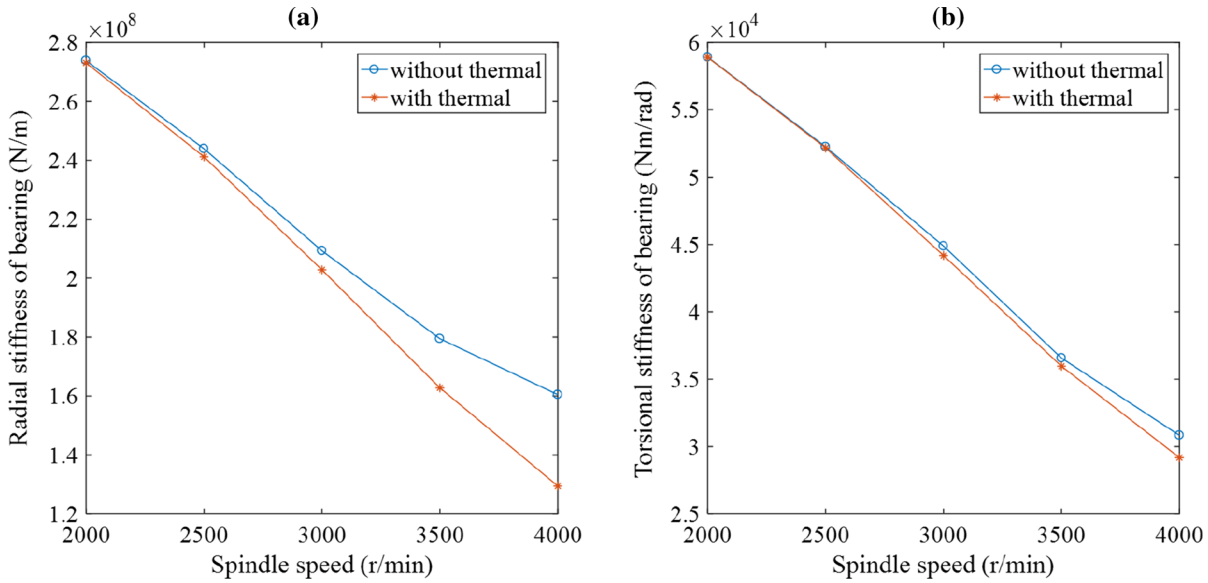

Fig. 14 Relationship between spindle speed and bearing stiffness

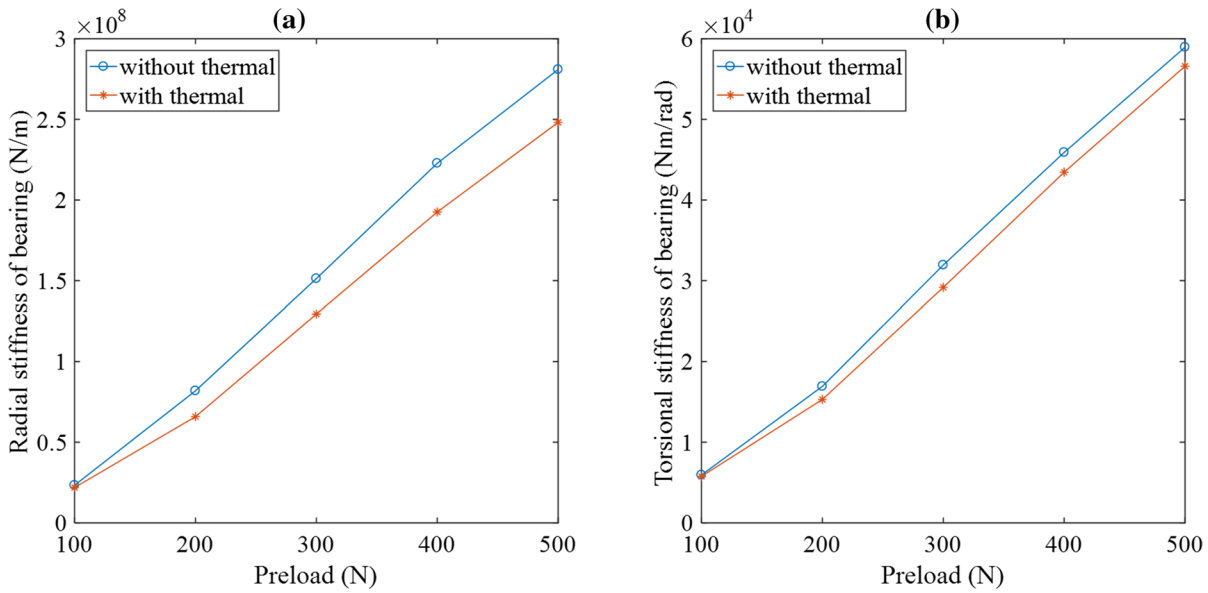

Fig. 15 Relationship between preload and bearing stiffness

reduction in the contact load between balls and raceways.

In Fig. 13, it can be seen the variation of contact angle and contact load with preload when the rotating speed is 4000 r/min with and without thermal deformation. The contact angle between balls and inner and outer raceways with thermal deformation is smaller than without thermal deformation. The contact angle of inner raceway decreases with the increase of preload, while the contact angle of outer raceway is opposite. This is mainly because the effect of centrifugal force is weakened by preload. The contact load between balls and inner and outer raceways with thermal deformation is smaller than that without thermal deformation, because the total thermal deformation between balls and inner and outer raceways is

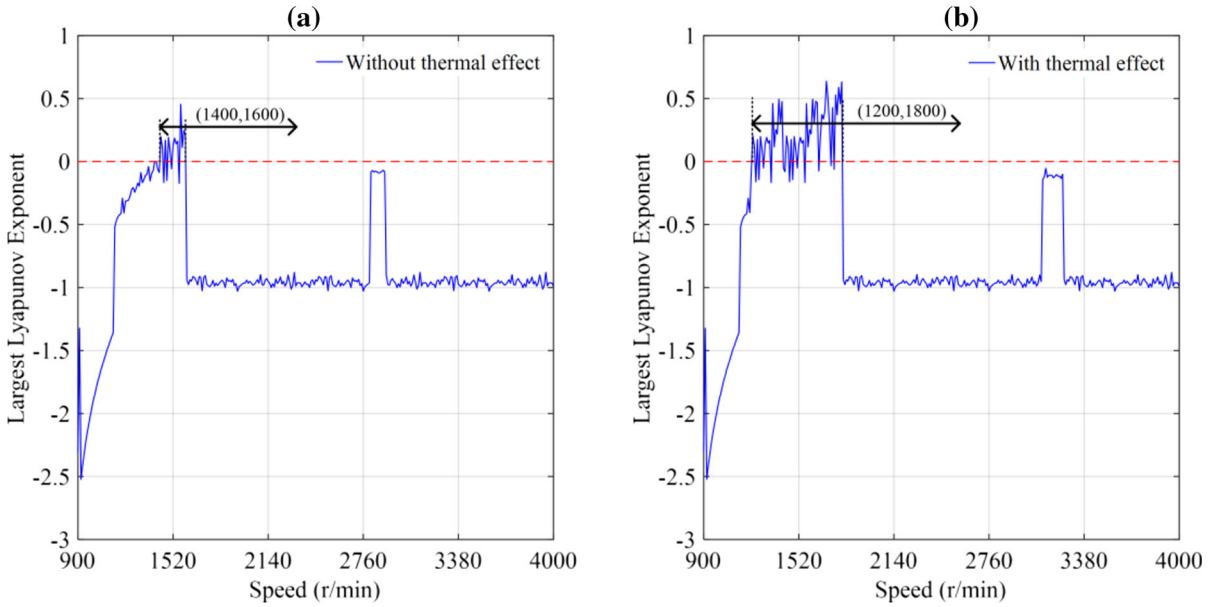

Fig. 16 The largest Lyapunov exponent of the CNC lathe spindle-bearing system

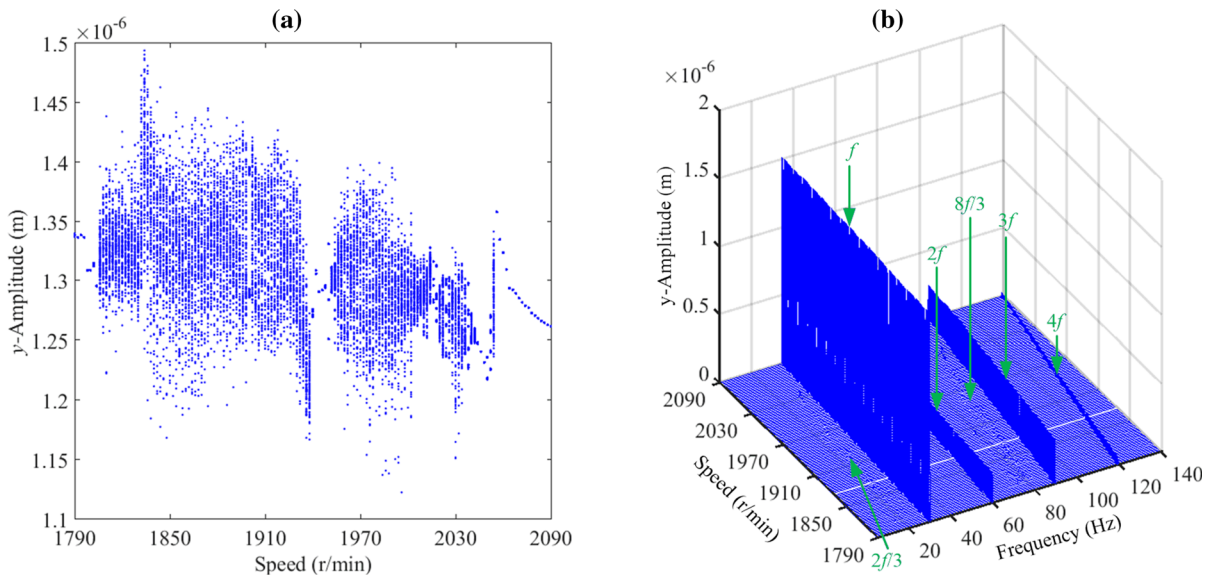

Fig. 17 Bifurcation diagram and 3-D spectrum of horizontal radial of shaft end in the spindle-bearing system. **a** Bifurcation diagram, **b** 3-D spectrum plot

negative, which will make balls and inner and outer raceways relaxed and lead to a decrease in contact load.

4.2 The influence of rotational speed and preload on bearing stiffness

The bearing stiffness will also be changed by the variation of contact angle and contact load between balls and inner and outer raceways. Figure 14 shows the variation trend of bearing stiffness with spindle

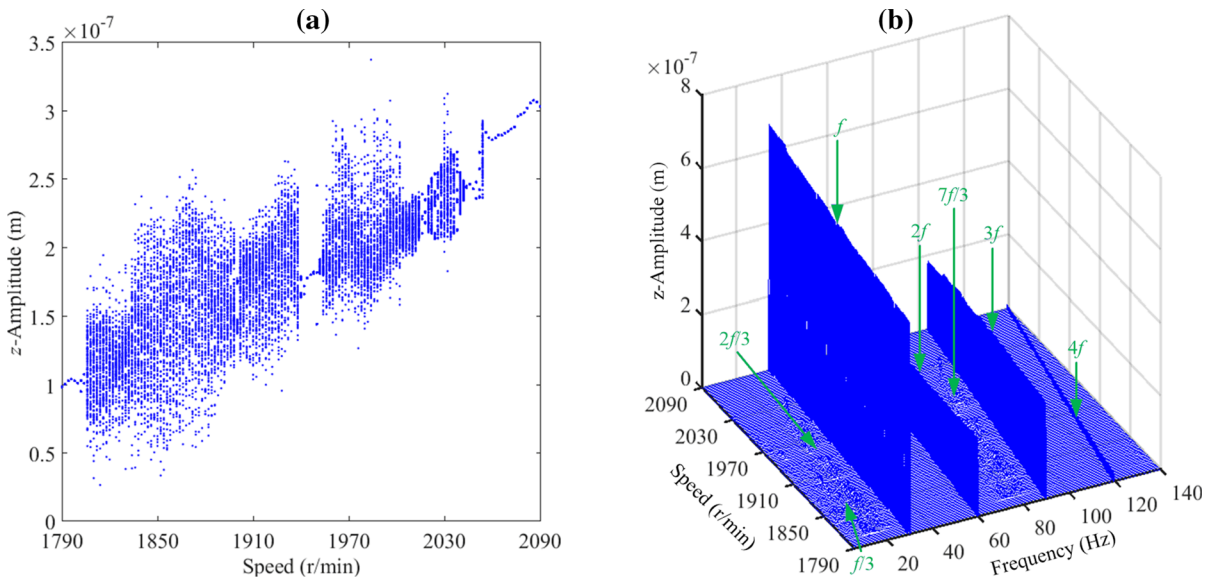

Fig. 18 Bifurcation diagram and 3-D spectrum of vertical radial of shaft end in the spindle-bearing system. **a** Bifurcation diagram, **b** 3-D spectrum plot

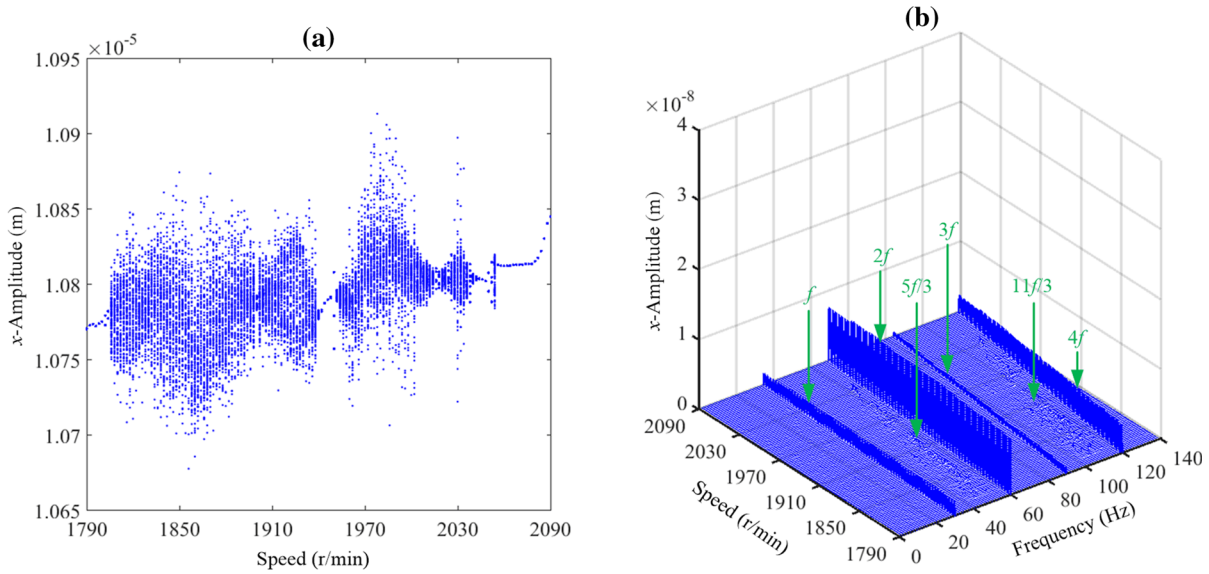

Fig. 19 Bifurcation diagram and 3-D spectrum of axial of shaft end in the spindle-bearing system. **a** Bifurcation diagram, **b** 3-D spectrum plot

speed when the preload is set to 500 N. With the increase of spindle speed, the bearing stiffness decreases gradually. This reflects the softening effect of rotational speed on stiffness. The bearing stiffness considering thermal deformation is smaller than that without thermal deformation. As can be seen from Fig. 12c and d, the contact load between balls and inner and outer raceways decreases by considering the thermal deformation of bearing parts, which leads to the decrease of bearing stiffness.

According to the variation trend of bearing stiffness with preload when the rotating speed is set to 4000 r/min. It can be seen from Fig. 15, the greater the bearing preload, the greater the bearing stiffness.

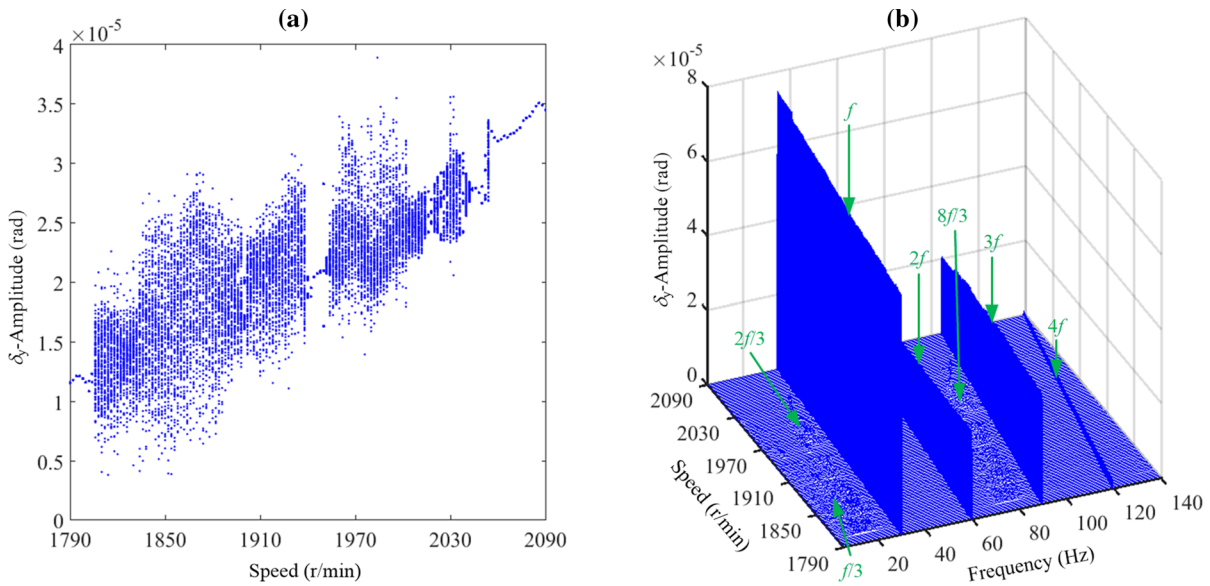

Fig. 20 Bifurcation diagram and 3-D spectrum of horizontal radial torsion of shaft end in the spindle-bearing system. **a** Bifurcation diagram, **b** 3-D spectrum plot

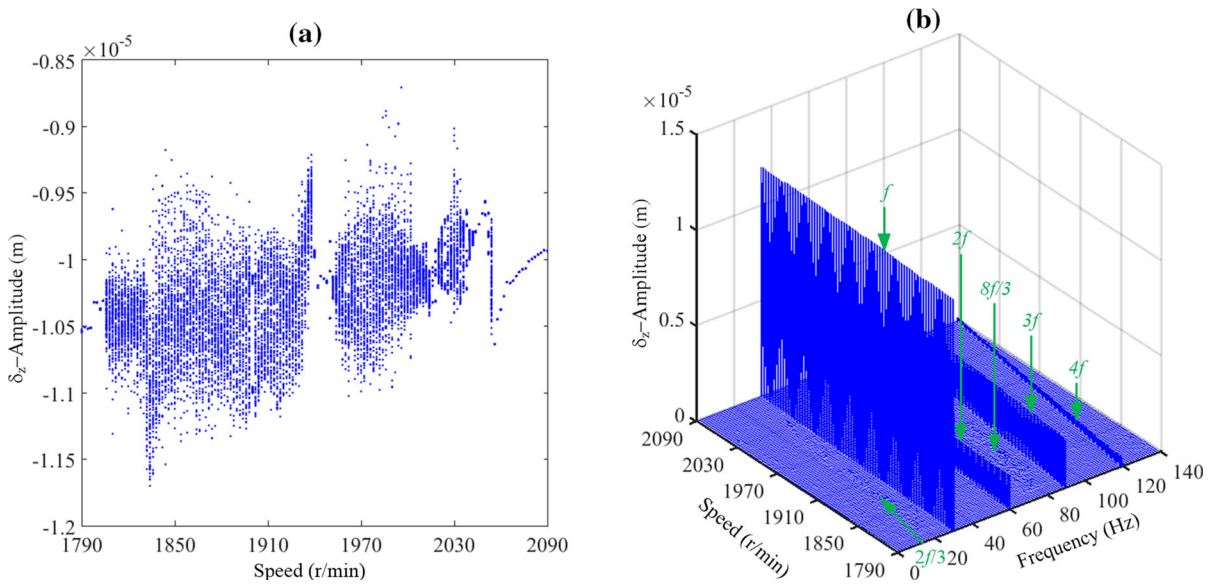

Fig. 21 Bifurcation diagram and 3-D spectrum of vertical radial torsion of shaft end in the spindle-bearing system. **a** Bifurcation diagram, **b** 3-D spectrum plot

However, the bearing stiffness considering thermal deformation is smaller than that without considering thermal deformation. The same reason is that the bearing parts generate thermal deformation. However, the total thermal deformation of balls and inner and outer raceways is negative, which results in lowing the bearing stiffness.

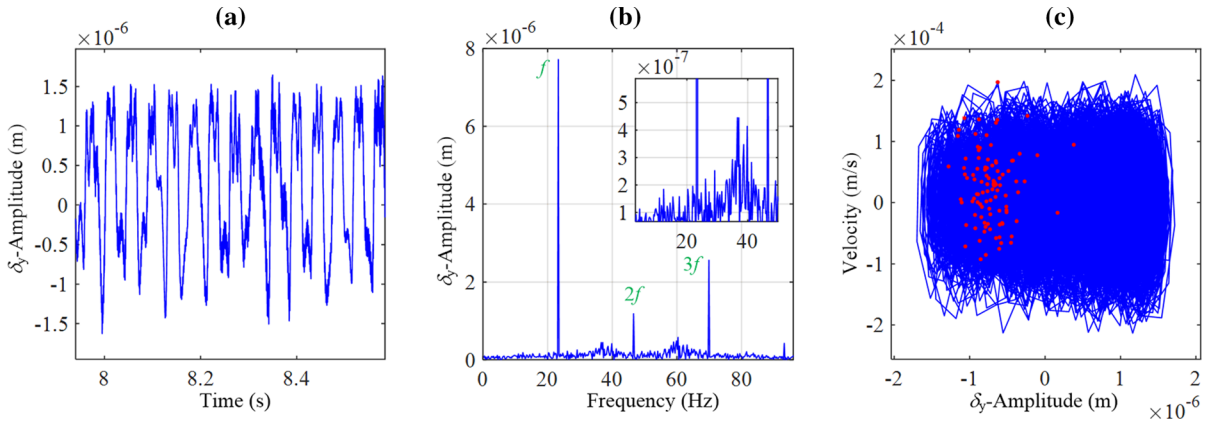

Fig. 22 Nonlinear responses at ω = 1400 r/min: **a** time history, **b** frequency spectrum, **c** phase plane diagram and Poincare section

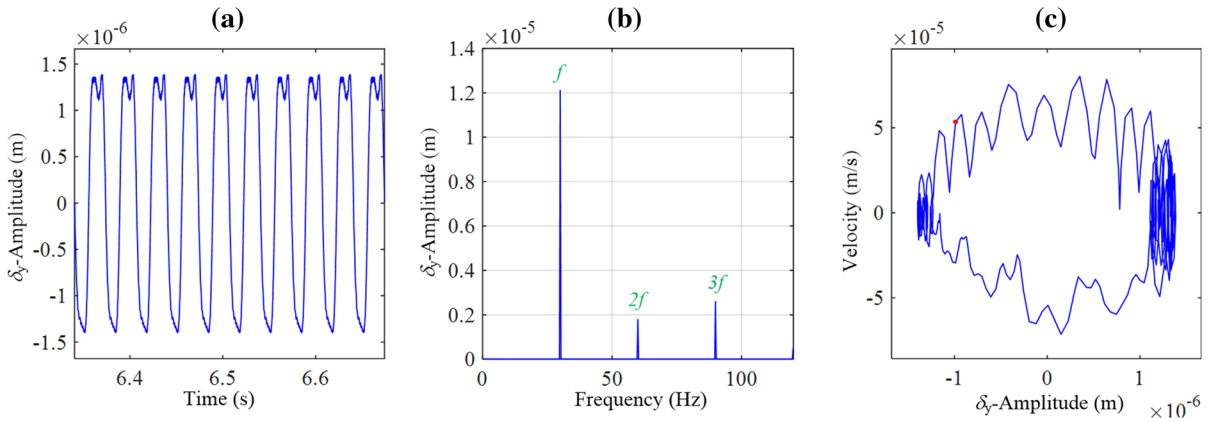

Fig. 23 Nonlinear responses at ω = 1800 r/min: **a** time history, **b** frequency spectrum, **c** phase plane diagram and Poincare section

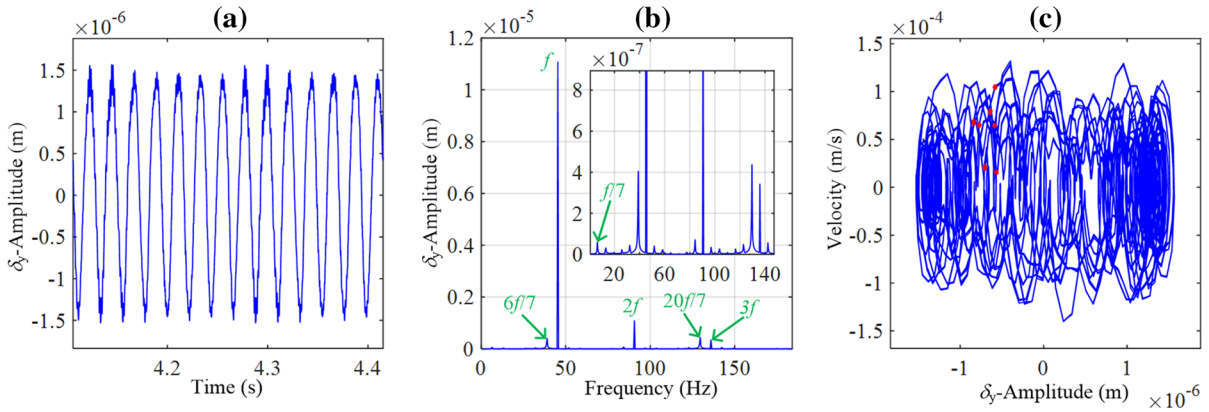

Fig. 24 Nonlinear responses at ω = 2720 r/min: **a** time history, **b** frequency spectrum, **c** phase plane diagram and Poincare section

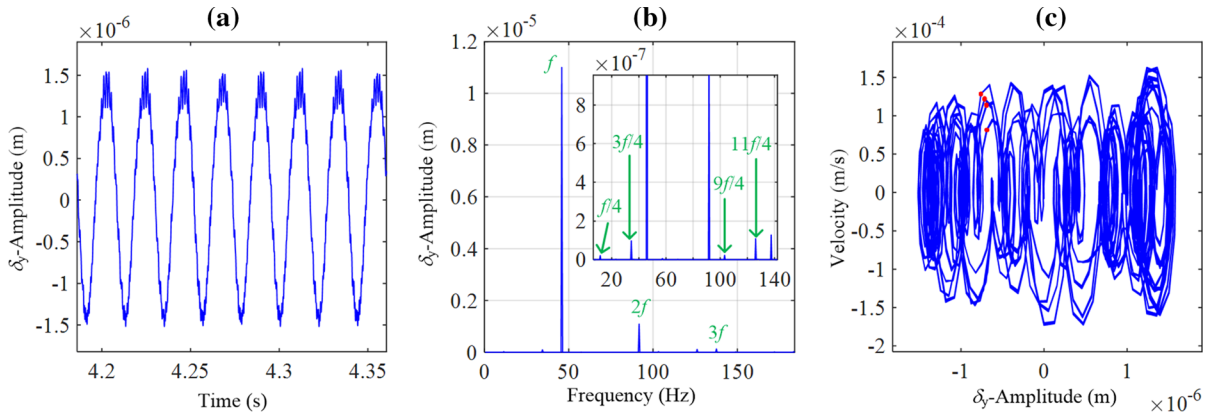

Fig. 25 Nonlinear responses at ω = 2754 r/min: **a** time history, **b** frequency spectrum, **c** phase plane diagram and Poincare section

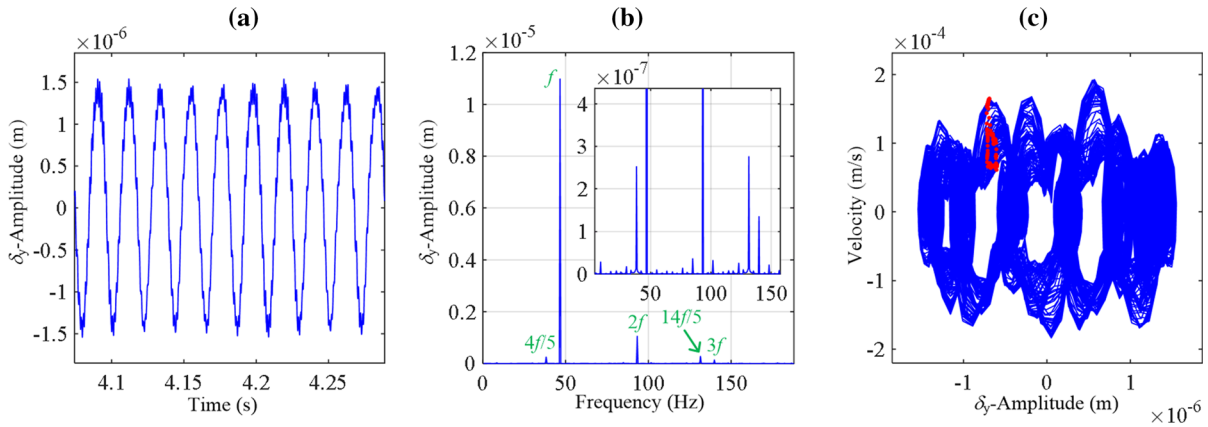

Fig. 26 Nonlinear responses at ω = 2800 r/min: **a** time history, **b** frequency spectrum, **c** phase plane diagram and Poincare section

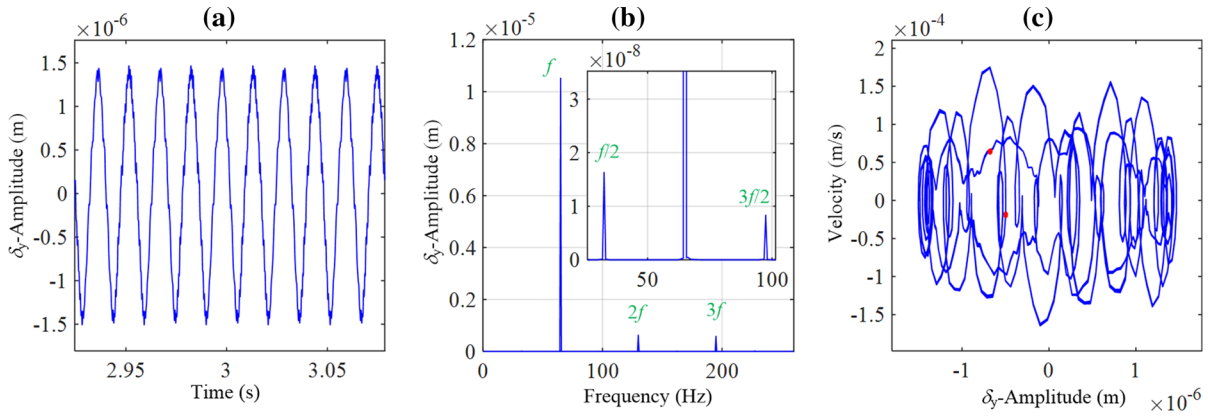

Fig. 27 Nonlinear responses at ω = 3900 r/min: **a** time history, **b** frequency spectrum, **c** phase plane diagram and Poincare section

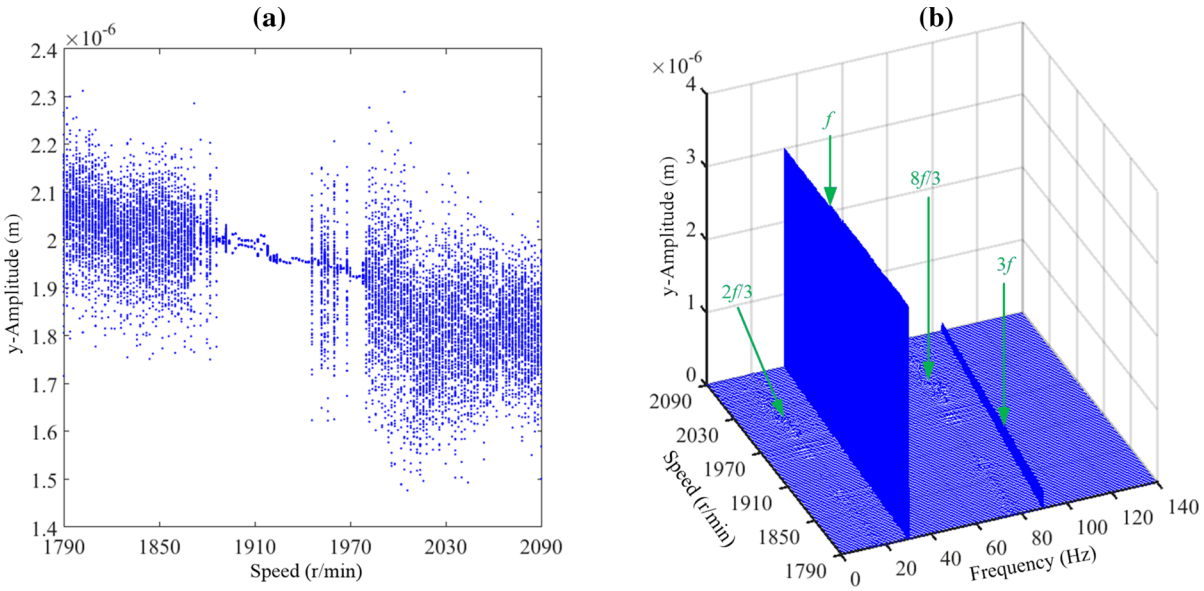

Fig. 28 Bifurcation diagram and 3-D spectrum of horizontal radial of shaft end in the spindle-bearing system. a Bifurcation diagram, b 3-D spectrum plot

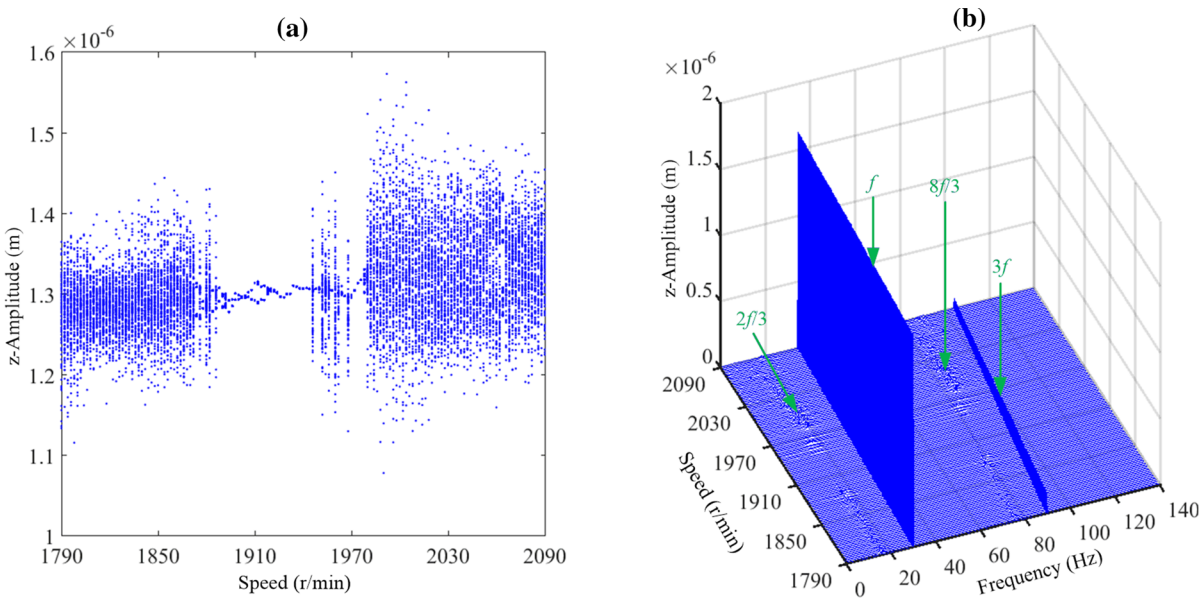

Fig. 29 Bifurcation diagram and 3-D spectrum of vertical radial of shaft end in the spindle-bearing system. a Bifurcation diagram, b 3-D spectrum plot

4.3 The stability analysis of system

As shown in Fig. 16, Lyapunov exponent is used to further study the influence of thermal effect on the stability of response of spindle-bearing system of CNC lathe. The Lyapunov exponents were similar to each other. When the thermal effect is not taken into account, the chaotic motion of the system appears between 1400 r /min and 1600 r /min. When thermal effects are taken into account, the chaotic motion of the system shifts to between 1200 r /min and 1800 r / min. This indicates that after considering the thermal

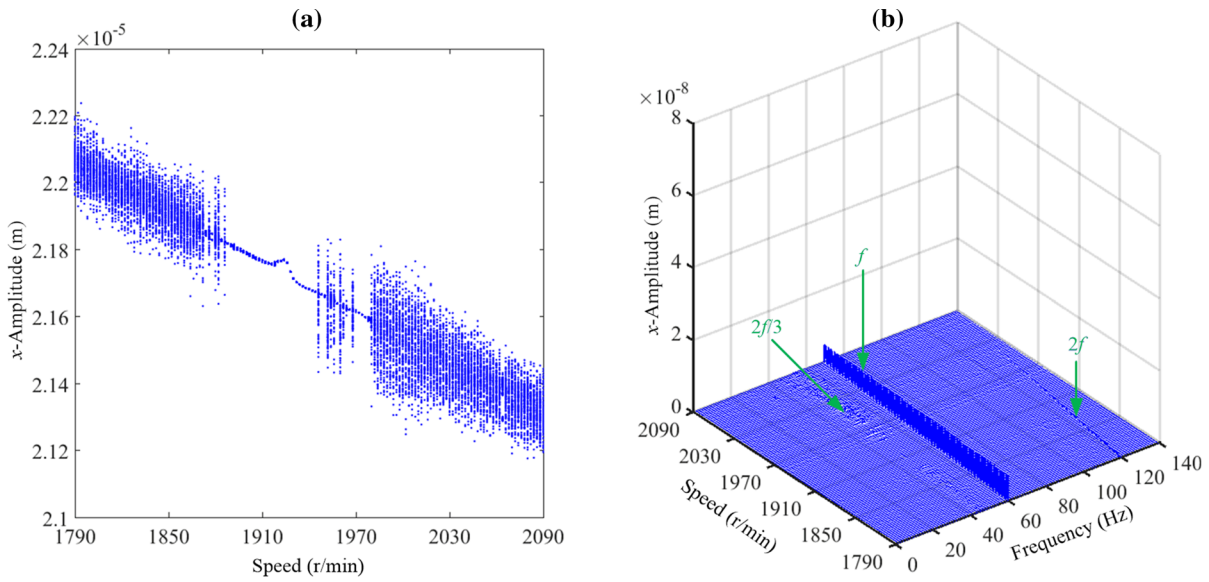

Fig. 30 Bifurcation diagram and 3-D spectrum of axial of shaft end in the spindle-bearing system. a Bifurcation diagram, b 3-D spectrum plot

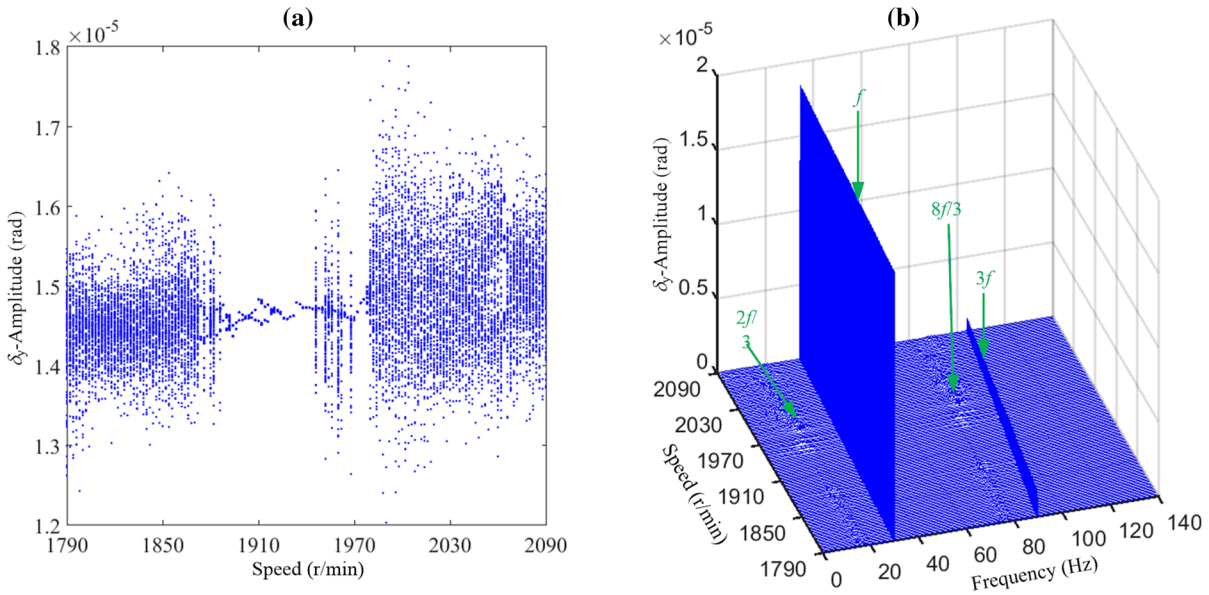

Fig. 31 Bifurcation diagram and 3-D spectrum of horizontal radial torsion of shaft end in the spindle-bearing system. a Bifurcation diagram, b 3-D spectrum plot

effect, with the increase of the rotational speed, the chaotic motion appears at an earlier rotational speed and the interval of the chaotic region increases.

4.4 The influence of rotational speed on dynamic characteristics of system without thermal effect

The pulley eccentricity is set to 5 *um*, and the rotational speed of spindle is limited to 1790 r /min to 2090 r /min without considering the thermal effect

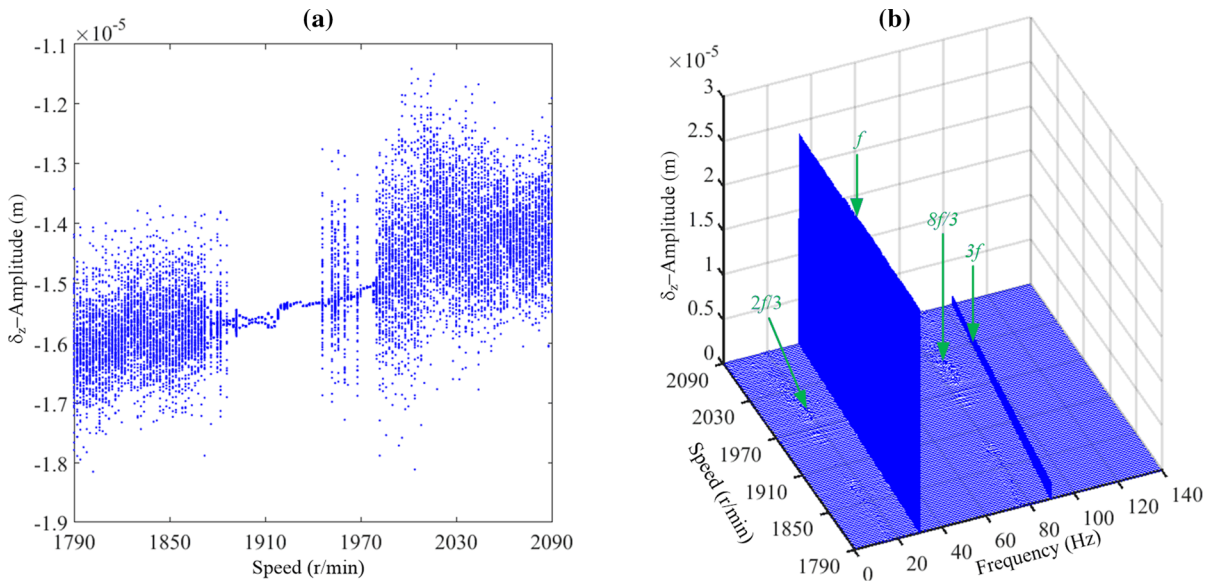

Fig. 32 Bifurcation diagram and 3-D spectrum of vertical radial torsion of shaft end in the spindle-bearing system. a Bifurcation diagram, b 3-D spectrum plot

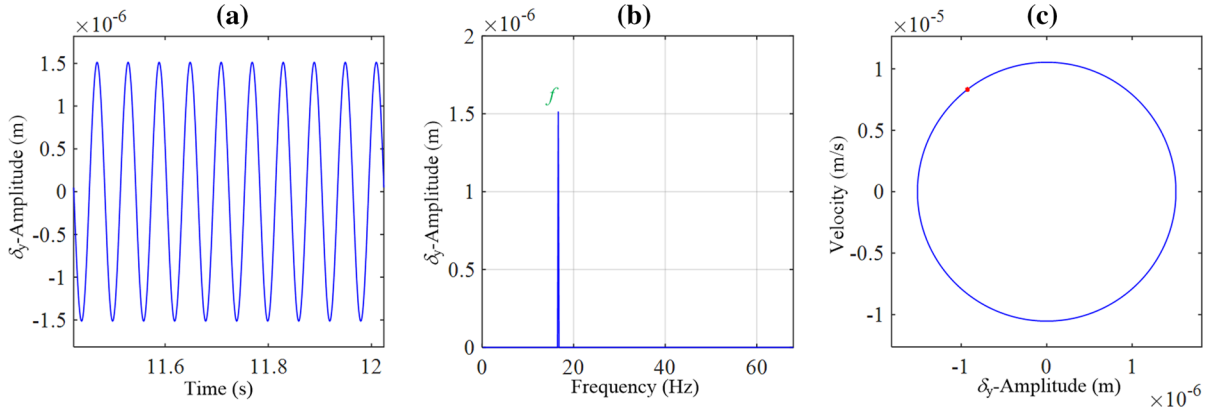

Fig. 33 Nonlinear responses at ω = 1000 r/min: **a** time history, **b** frequency spectrum, **c** phase plane diagram and Poincare section

of spindle-bearing system of CNC lathe. The bifurcation diagrams and 3-D spectrum plots of shaft end of CNC lathe spindle-bearing system with five DOF are shown in Figs. 17, 18, 19, 20 and 21. The comparison of five directional bifurcation diagrams and three-dimensional spectrum plots show that the variation trend of motion state and frequency composition at the shaft end are basically the same, but the response amplitudes are different in different degrees of freedom.

In order to study the vibration characteristics of shaft end of CNC lathe spindle-bearing system, the horizontal radial degree of freedom of shaft end will be regarded as an example in the following. The nonlinear dynamic behaviors of system responses are investigated through the time history, frequency spectrum, phase plane diagram and Poincare section. With the increase of rotational speed, the system experiences chaotic motion, single-periodic, 7T-periodic, 4T-periodic, quasi-periodic, 2T-periodic motions shown in Figs. 22, 23, 24, 25, 26, and 27. In Fig. 22, chaotic motion can be seen based on the time domain response is no longer periodically changing, the frequency domain presents continuous spectrum, and the phase diagram and Poincare section are full of a large number of discrete points. The system presents

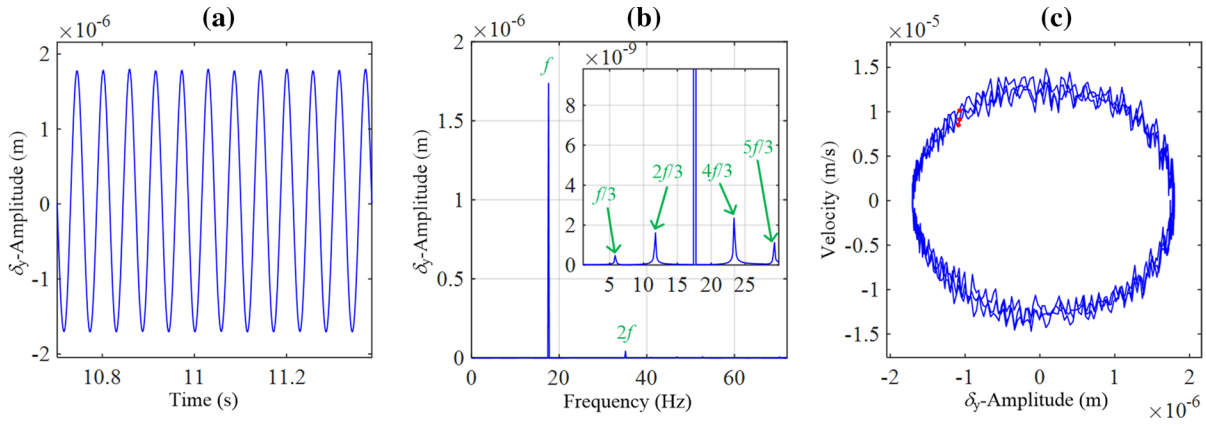

Fig. 34 Nonlinear responses at ω = 1056 r/min: **a** time history, **b** frequency spectrum, **c** phase plane diagram and Poincare section

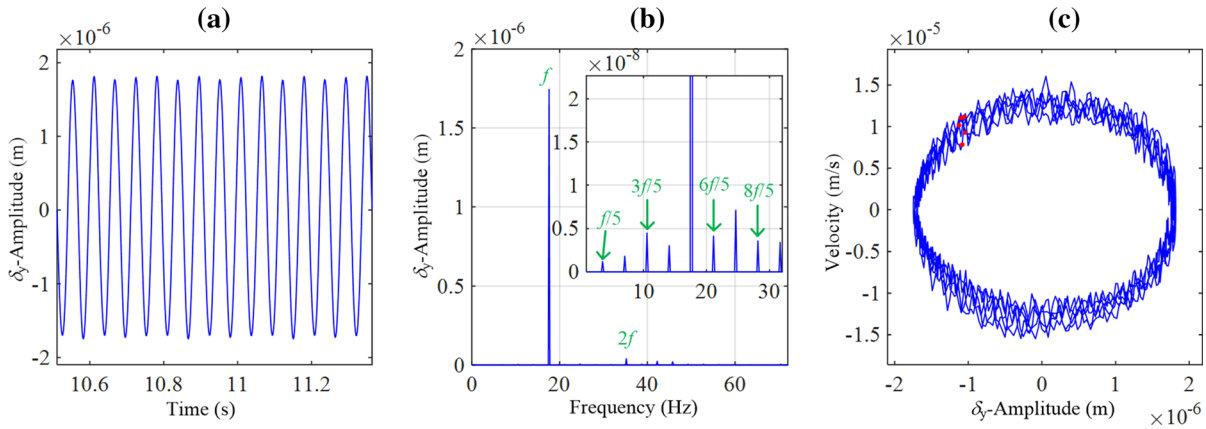

Fig. 35 Nonlinear responses at ω = 1058 r/min: **a** time history, **b** frequency spectrum, **c** phase plane diagram and Poincare section

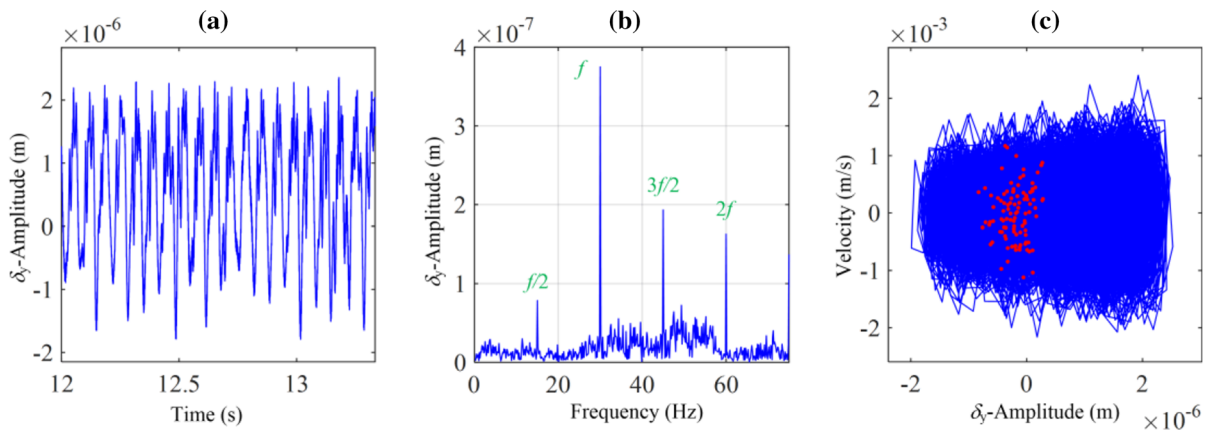

Fig. 36 Nonlinear responses at ω = 1800 r/min: **a** time history, **b** frequency spectrum, **c** phase plane diagram and Poincare section

single-periodic, 7T-periodic, 4T-periodic, and 2T-periodic motions, which can be determined by the frequency demultiplication component and discrete Poincare points in Figs. 23, 24, 25 and 27. The quasi-periodic motion appears at rotational speed reaches 2800 r/min; it can be seen from the continuous

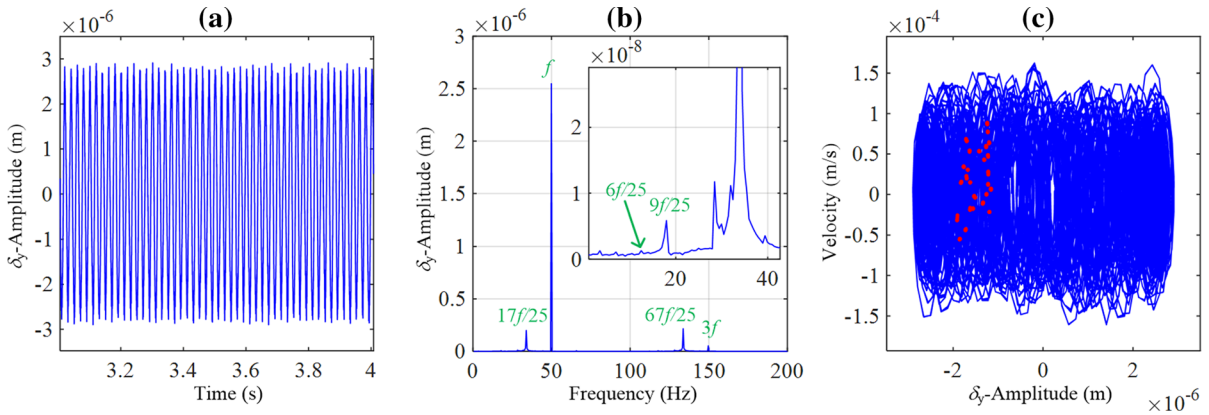

Fig. 37 Nonlinear responses at ω = 2996 r/min: **a** time history, **b** frequency spectrum, **c** phase plane diagram and Poincare section

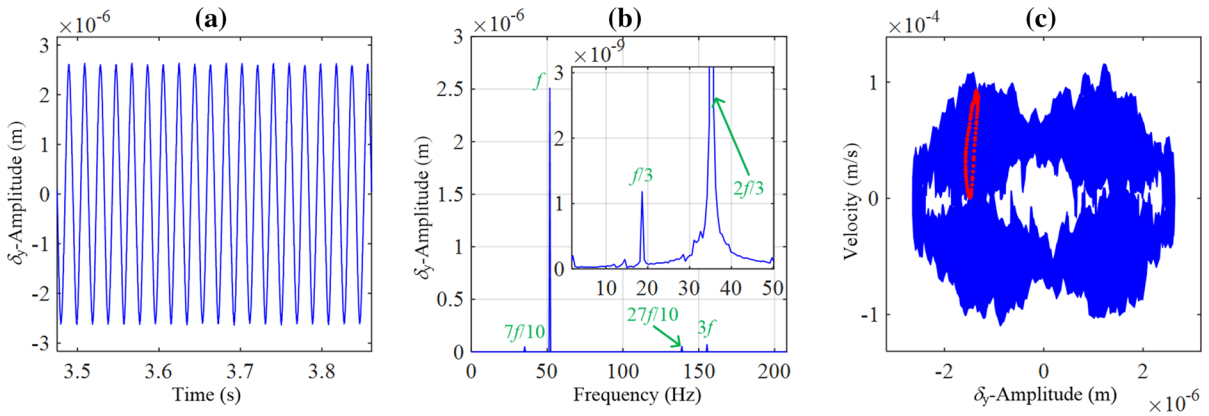

Fig. 38 Nonlinear responses at ω = 3110 r/min: **a** time history, **b** frequency spectrum, **c** phase plane diagram and Poincare section

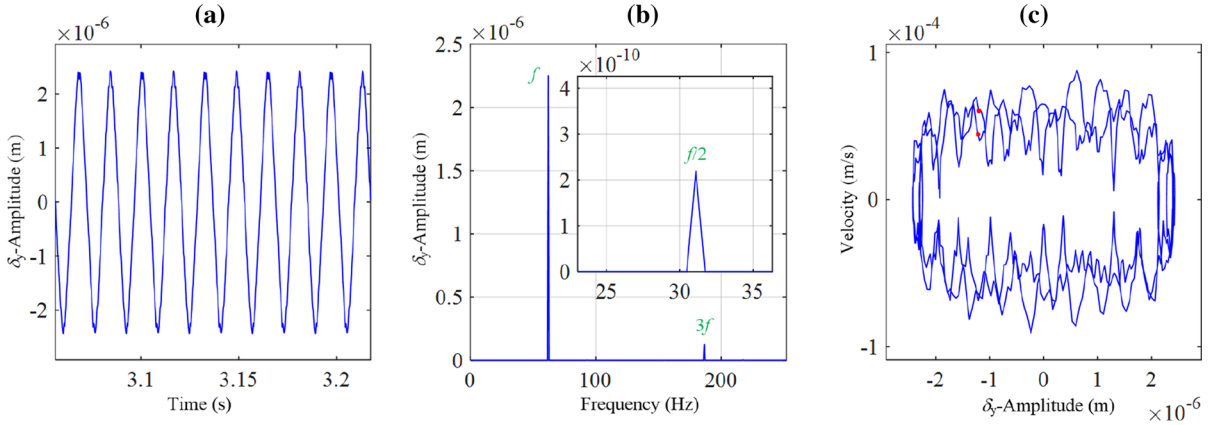

Fig. 39 Nonlinear responses at ω = 3732 r/min: **a** time history, **b** frequency spectrum, **c** phase plane diagram and Poincare section

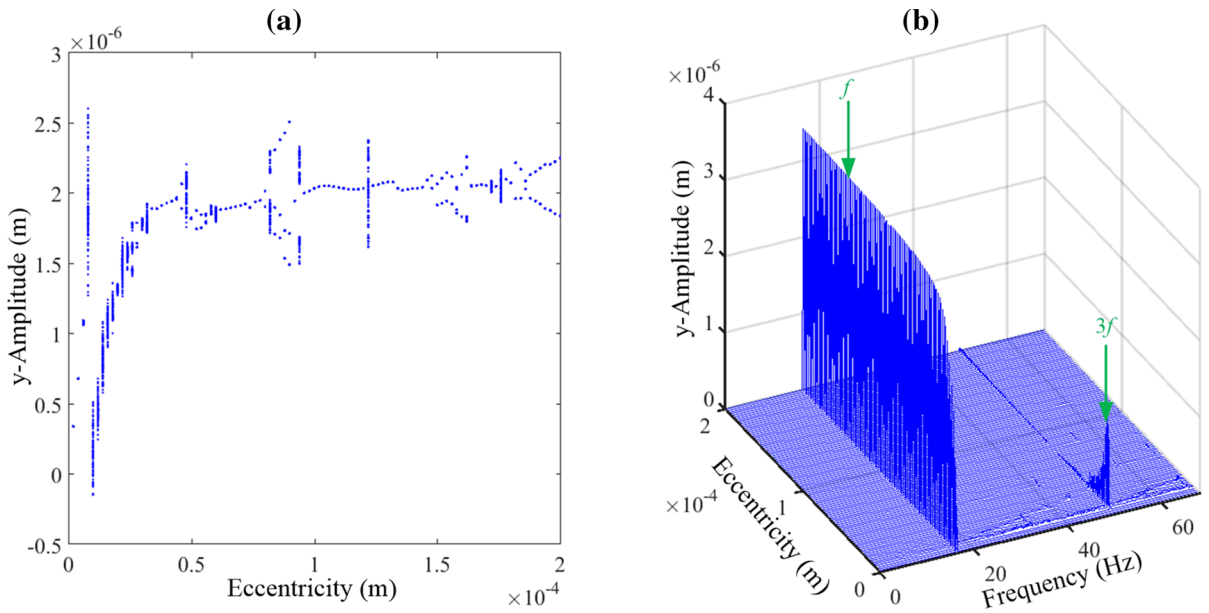

Fig. 40 Bifurcation diagram and 3-D spectrum of horizontal radial torsion of shaft end in the spindle-bearing system at ω = 1000 r/min. **a** Bifurcation diagram, **b** 3-D spectrum plot

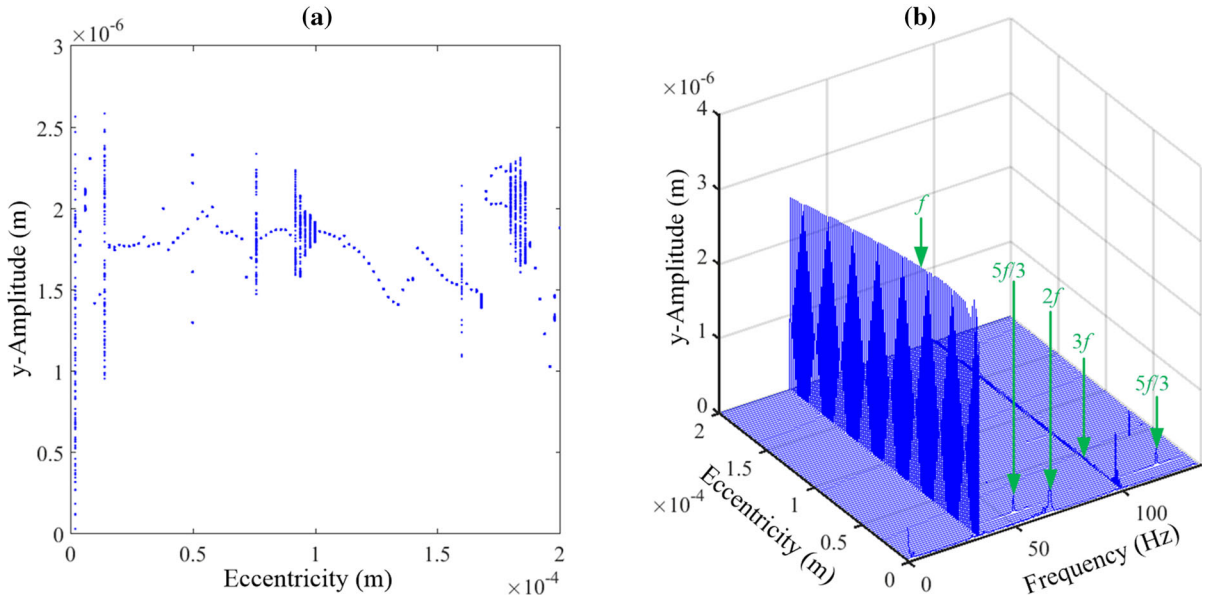

Fig. 41 Bifurcation diagram and 3-D spectrum of horizontal radial torsion of shaft end in the spindle-bearing system at ω = 2000 r/min. **a** Bifurcation diagram, **b** 3-D spectrum plot

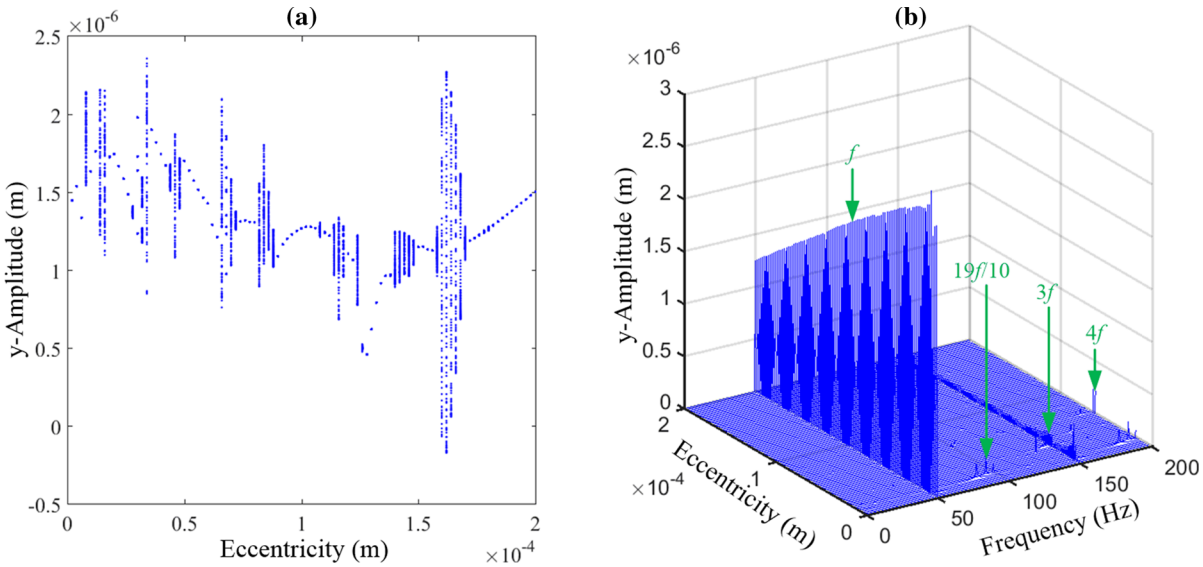

Fig. 42 Bifurcation diagram and 3-D spectrum of horizontal radial torsion of shaft end in the spindle-bearing system at ω = 3000 r/min. **a** Bifurcation diagram, **b** 3-D spectrum plot

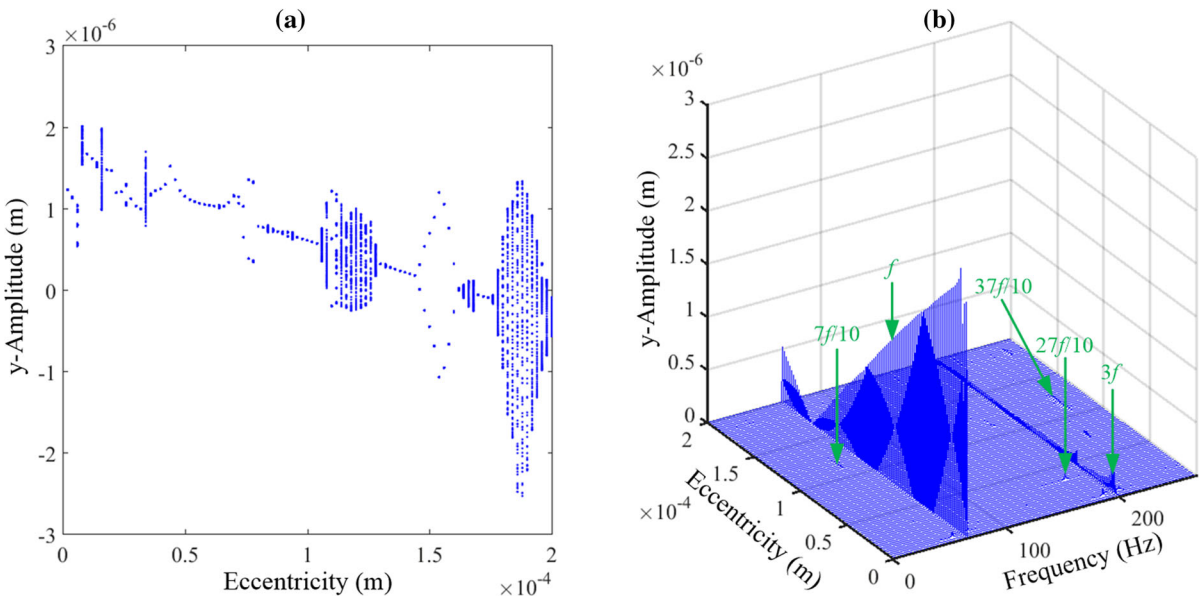

Fig. 43 Bifurcation diagram and 3-D spectrum of horizontal radial torsion of shaft end in the spindle-bearing system at ω = 4000 r/min. **a** Bifurcation diagram, **b** 3-D spectrum plot

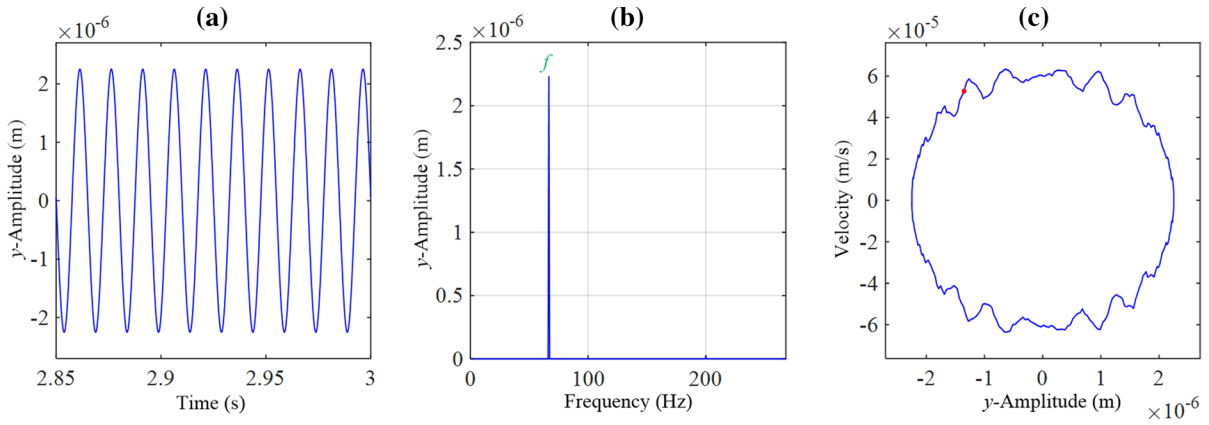

Fig. 44 Nonlinear responses at(Ec = 2 *um*): **a** time history, **b** frequency spectrum, **c** phase plane diagram and Poincare section

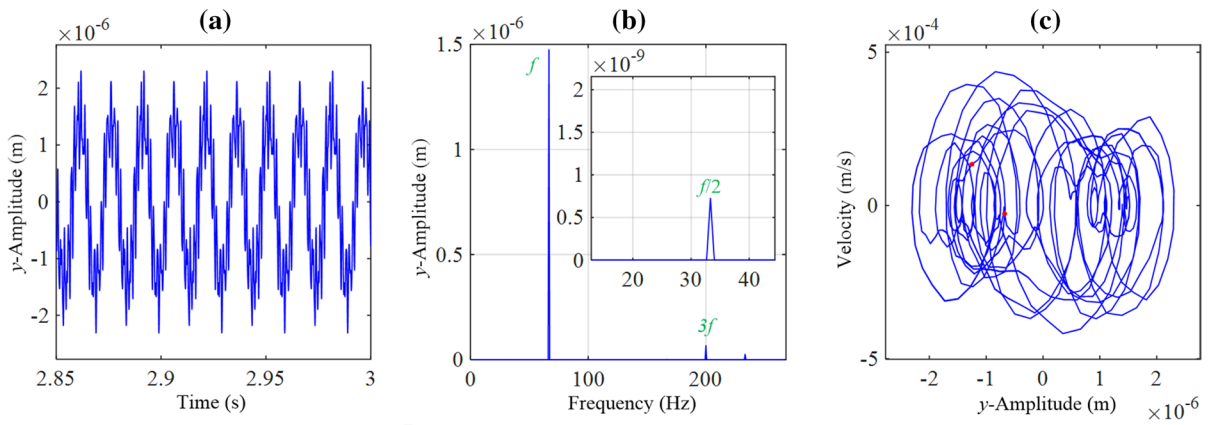

Fig. 45 Nonlinear responses at(Ec = 76 *um*): **a** time history, **b** frequency spectrum, **c** phase plane diagram and Poincare section

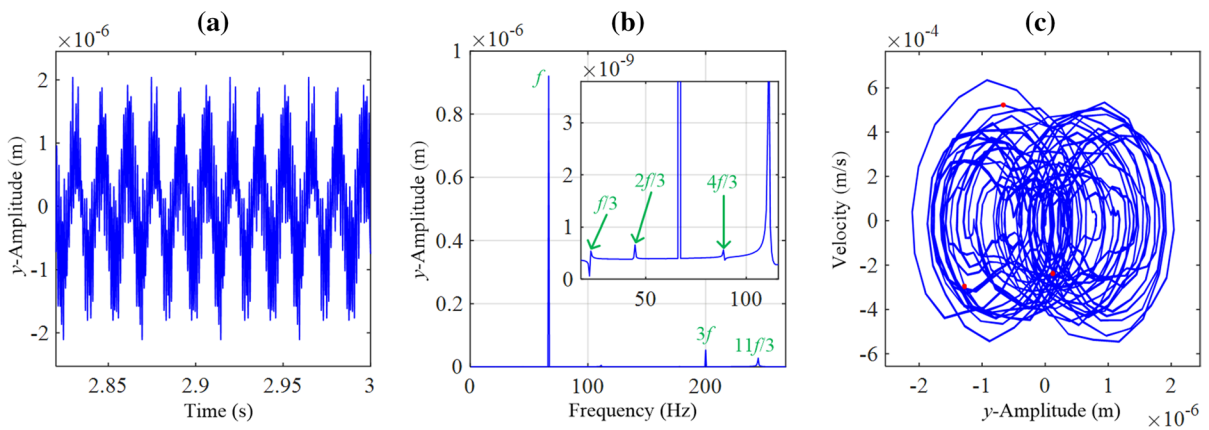

Fig. 46 Nonlinear responses at(Ec = 112 *um*): **a** time history, **b** frequency spectrum, **c** phase plane diagram and Poincare section

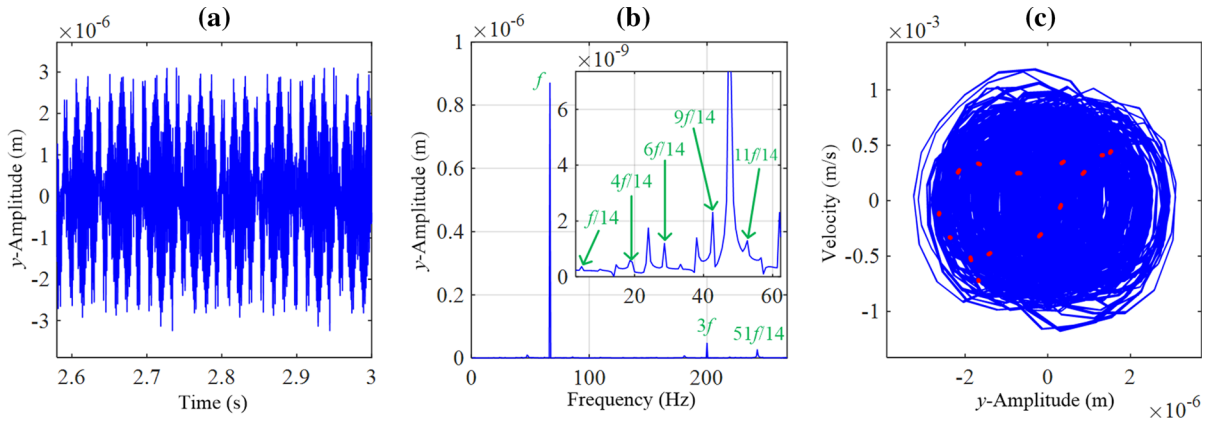

Fig. 47 Nonlinear responses at(Ec = 114 *um*): **a** time history, **b** frequency spectrum, **c** phase plane diagram and Poincare section

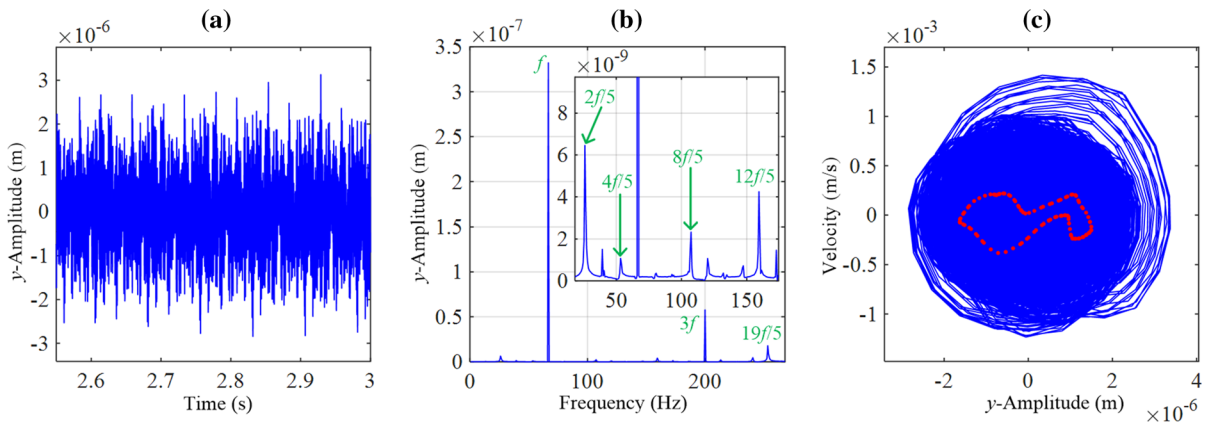

Fig. 48 Nonlinear responses at(Ec = 190 *um*): **a** time history, **b** frequency spectrum, **c** phase plane diagram and Poincare section

frequency components in the spectrum plot and a number of Poincare points form a closed loop in Fig. 26.

4.5 The dynamic characteristics of system with thermal effect

4.5.1 The influence of rotational speed on dynamic characteristics of system

In order to investigate the influence of thermal effect on CNC lathe spindle-bearing system, the bifurcation diagrams and 3-D spectrum plots of five DOF of shaft end are employed shown in Figs. 28, 29, 30, 31 and 32. Similarly, the pulley eccentricity is set to 5 *um* and the rotational speed of spindle is limited to 1790 r/min to 2090 r/min. The variation trend of motion state and frequency composition at the shaft end are similar, but the response amplitudes are different in different degrees of freedom. Comparing with the above situation without thermal effect shown in Figs. 17, 18, 19, 20 and 21, the response amplitude of system considering thermal effect is significantly larger than the system without thermal effect. This is due to thermal effect causes bearing stiffness to decrease, which increases the response of system.

In order to investigate the influence of thermal effect on the vibration characteristics of shaft end of CNC lathe spindle-bearing system, the horizontal radial degree of freedom of shaft end taken as an example for analysis. Figures 33, 34, 35, 36, 37, 38 and 39 demonstrate the time history curve, frequency spectrum plot, phase plane diagrams and Poincare sections under different rotational speeds. With the increase of rotational speed, the system exhibits single-periodic, 3T-periodic, 5T-periodic, chaotic

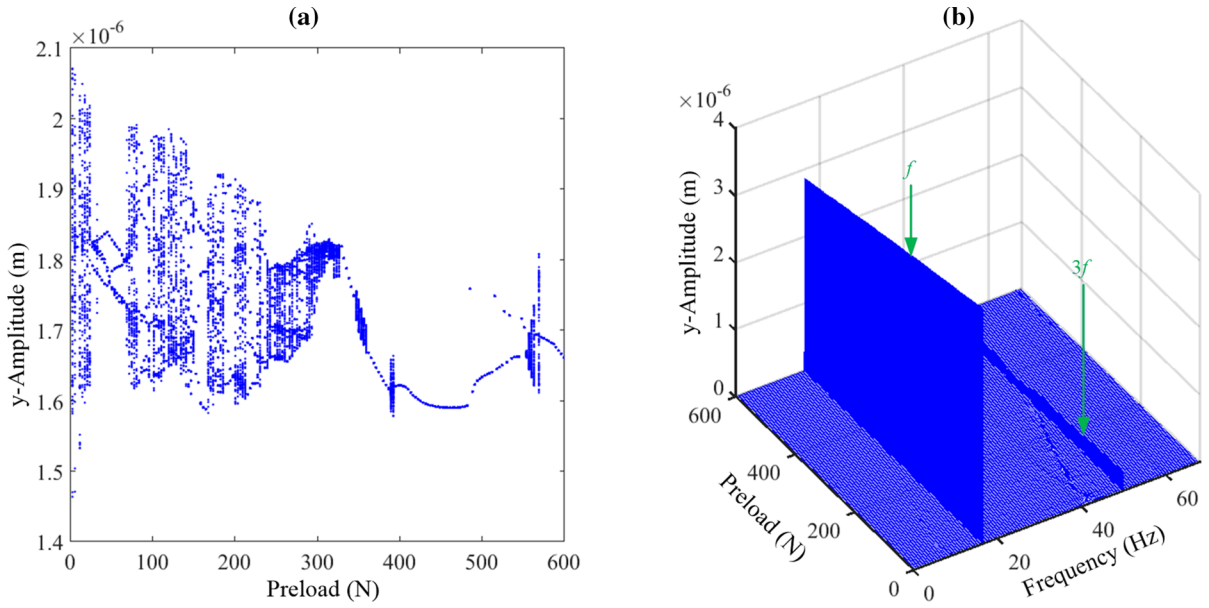

Fig. 49 Bifurcation diagram and 3-D spectrum of horizontal radial torsion of shaft end in the spindle-bearing system at ω = 1000 r/min. a Bifurcation diagram, b 3-D spectrum plot

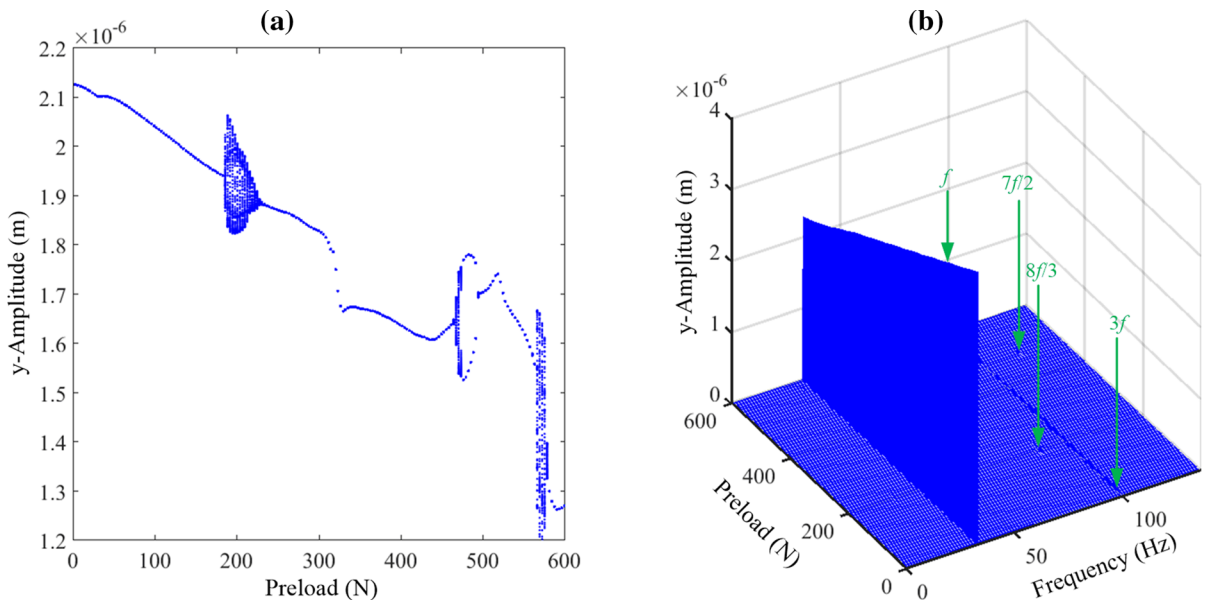

Fig. 50 Bifurcation diagram and 3-D spectrum of horizontal radial torsion of shaft end in the spindle-bearing system at ω = 2000 r/min. **a** Bifurcation diagram, **b** 3-D spectrum plot

motion, 25T-periodic, quasi-periodic and 2T-periodic motions. The 5T-periodic motion occurs as shown in Fig. 35 when rotational speed is increased to 1058 r/min, which can be determined by $f/5$ frequency demultiplication component and 5 discrete Poincare points. The chaotic motion in Fig. 36 is determined based on the time-domain response without periodic changes, the continuous spectral components and the phase diagram and Poincare section are full of a large number of discrete points. In the same way, we can identify the motions in Figs. 33, 34, 37 and 39 as single periodic, 3T-periodic, 25T-periodic and 2T-periodic

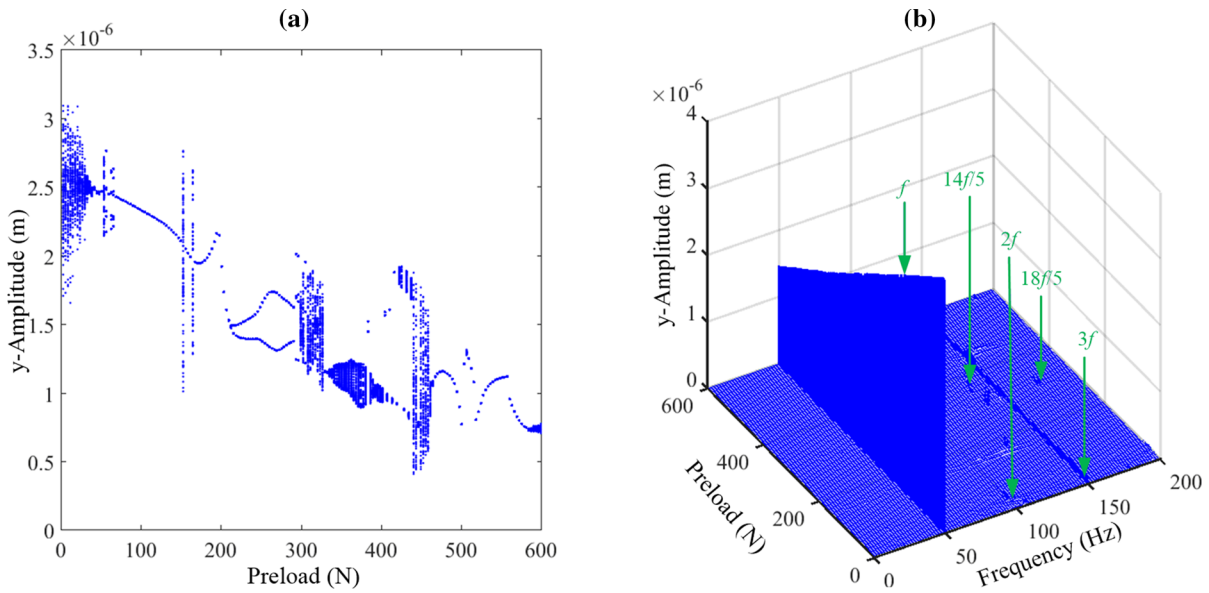

Fig. 51 Bifurcation diagram and 3-D spectrum of horizontal radial torsion of shaft end in the spindle-bearing system at ω = 3000 r/min. **a** Bifurcation diagram, **b** 3-D spectrum plot

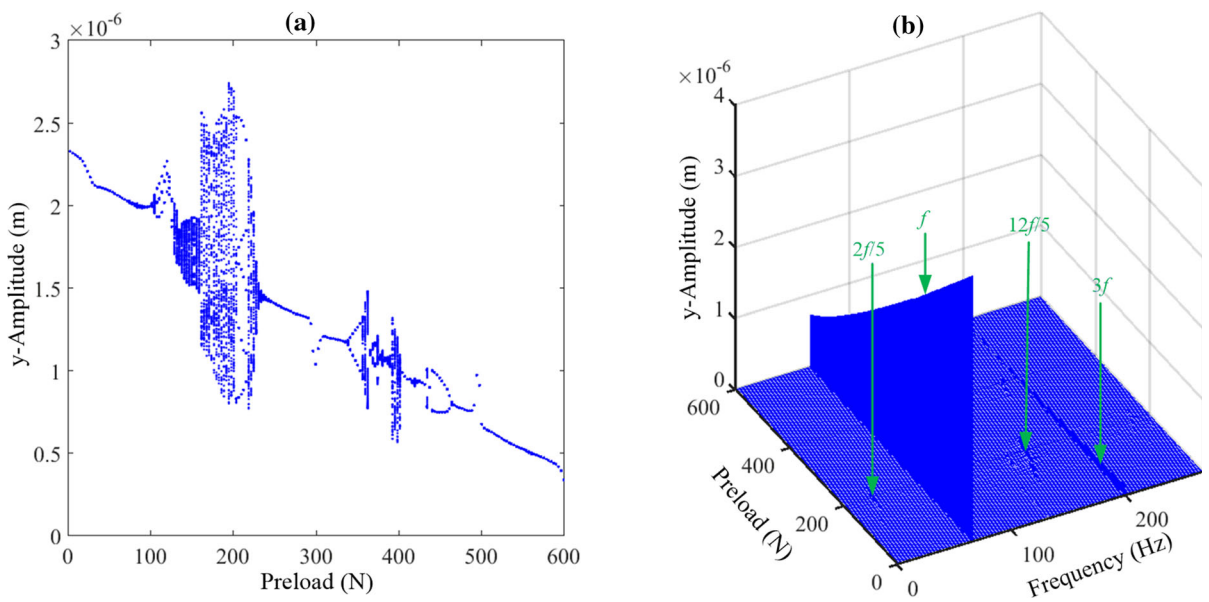

Fig. 52 Bifurcation diagram and 3-D spectrum of horizontal radial torsion of shaft end in the spindle-bearing system at ω = 4000 r/min. **a** Bifurcation diagram, **b** 3-D spectrum plot

respectively. As shown in the frequency spectrum and Poincare section in Fig. 38, when the rotation speed is 3110 rad/min, an obvious quasi-periodic motion appears, which can be seen from the continuous frequency components and a number of Poincare points form a closed loop.

4.5.2 The influence of pulley eccentricity on dynamic characteristics of system

From the model of CNC lathe spindle-bearing system considering thermal effect, it can be found that the eccentric load of pulley is used as excitation, then the

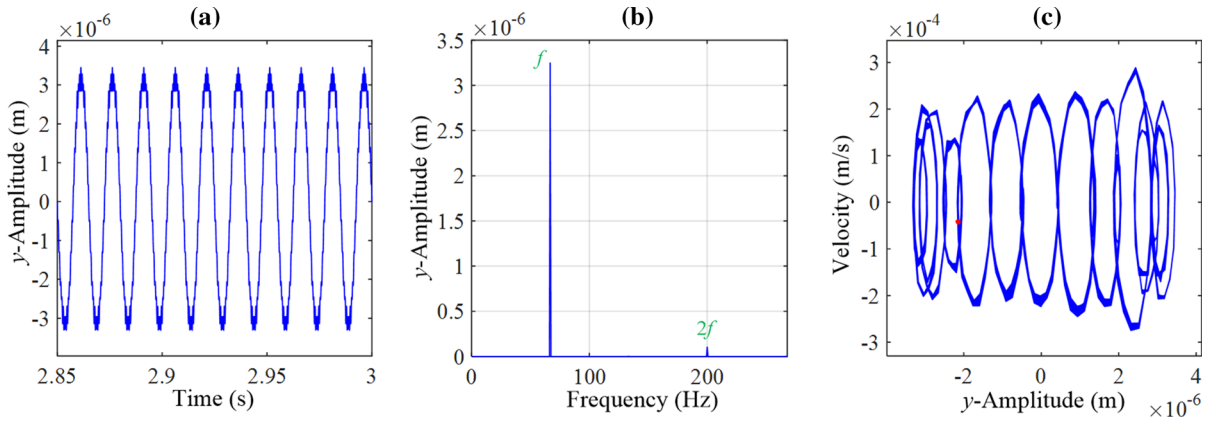

Fig. 53 Nonlinear responses at (Preload = 60 N): **a** time history, **b** frequency spectrum, **c** phase plane diagram and Poincare section

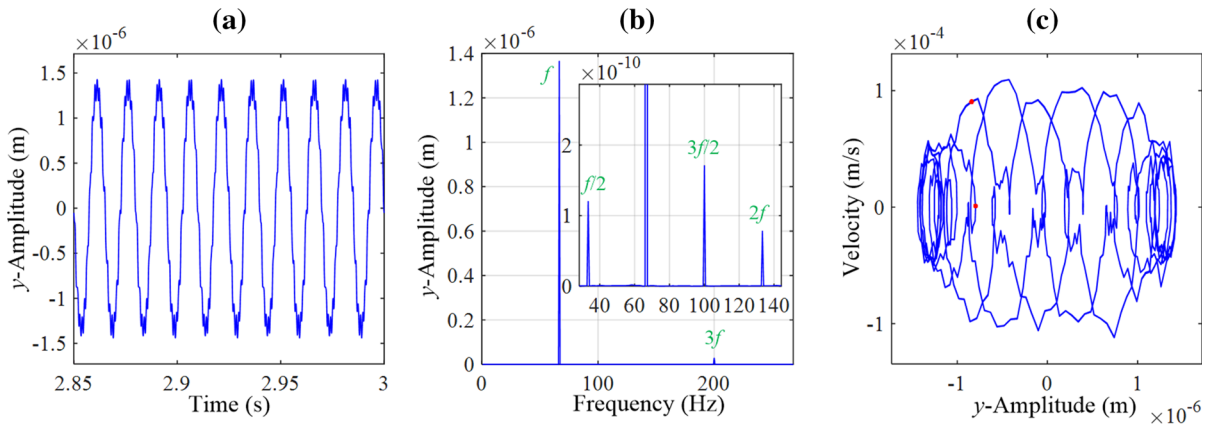

Fig. 54 Nonlinear responses at (Preload = 117 N): **a** time history, **b** frequency spectrum, **c** phase plane diagram and Poincare section

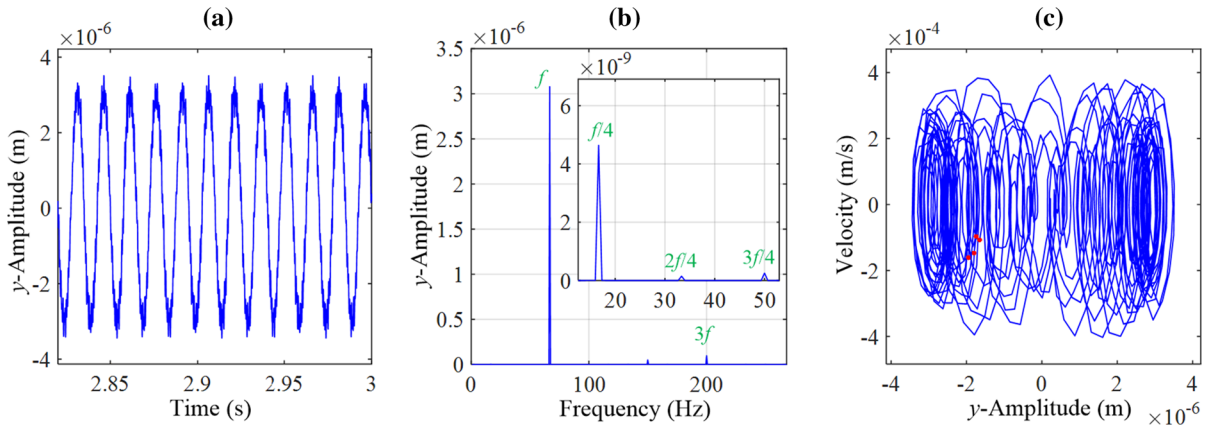

Fig. 55 Nonlinear responses at (Preload = 201 N): **a** time history, **b** frequency spectrum, **c** phase plane diagram and Poincare section

eccentricity will affect the dynamic behaviors of system. Therefore, the range of eccentricity is set at 2 to 200 *um* to investigate the nonlinear characteristics of system. Figures 40, 41, 42 and 43 depict the horizontal radial bifurcation diagrams and 3-D spectrum diagrams of shaft end at rotational speeds of 1000

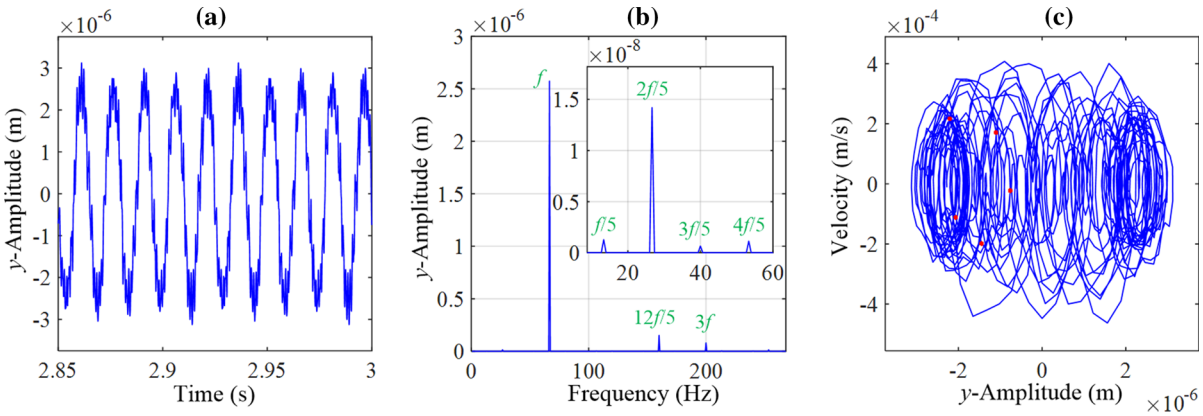

Fig. 56 Nonlinear responses at (Preload = 207 N): **a** time history, **b** frequency spectrum, **c** phase plane diagram and Poincare section

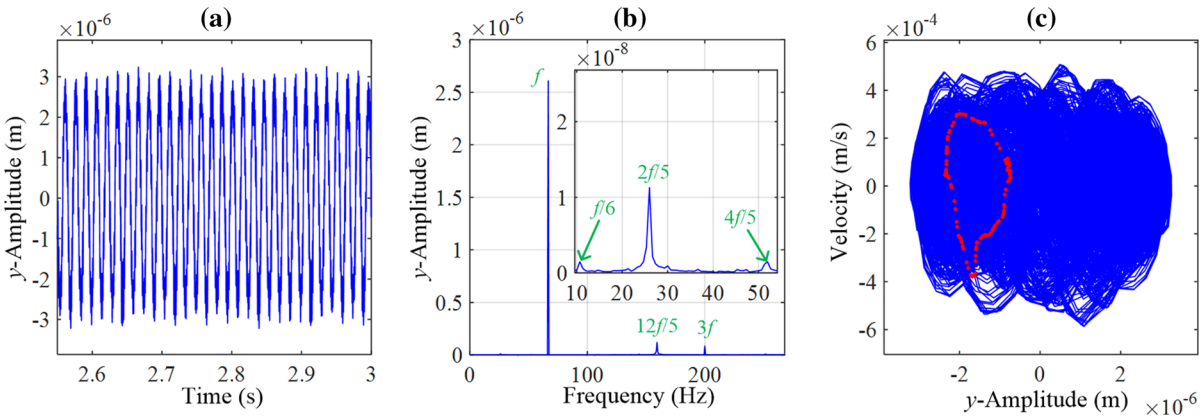

Fig. 57 Nonlinear responses at (Preload = 450 N): **a** time history, **b** frequency spectrum, **c** phase plane diagram and Poincare section

r/min, 2000 r/min, 3000 r/min, 4000 r/min, respectively. With the increase of spindle speed, the vibration system presents single-periodic, double-periodic, multiple-periodic and quasi-periodic motions.

Figures 44, 45, 46, 47 and 48 depict the change of motion state of shaft end of CNC lathe spindle-bearing system shown in Fig. 43 at different eccentricity amounts when the spindle speed is 4000 r/min. The system will undergo single-periodic, 2T-periodic, 3T-periodic, 14-periodic and quasi-periodic motions accordingly under the eccentricity is 2 *um*, 76 *um*, 112 *um*, 114 *um* and 190 *um*, respectively.

4.5.3 The influence of bearing preload on dynamic characteristics of system

Bearing preload will affect the contact deformation and load distribution of bearing parts, thus affecting the contact angle between balls and inner and outer raceways, bearing heat generation, bearing stiffness and even the dynamic behaviors of the whole system. Therefore, the preload will play an important role in CNC lathe spindle-bearing system. In order to investigate the dynamic nonlinear characteristics of system, the range of preload is set from 0 to 600 N. Figures 49, 50, 51 and 52 depict the horizontal radial bifurcation diagrams and 3-D spectrum diagrams of shaft end at rotational speeds of 1000 r/min, 2000 r/min, 3000 r/min, 4000 r/min, respectively. With the increasing of spindle speed, the vibration system presents rich nonlinear behaviors.

Figures 53, 54, 55, 56 and 57 depict the change of the motion state of shaft end shown in Fig. 52 at different preloads when the spindle speed is 4000 r/min. The system will undergo single-periodic, 2T-periodic, 4T-periodic, 5T-periodic and quasi-periodic motions accordingly, when the preload is 60 N, 117 N, 136 N, 140 N and 300 N, respectively.

5 Conclusions

The dynamic performance of spindle-bearing system is very important to the machining accuracy and working stability of CNC lathe. Therefore, a comprehensive dynamic model of CNC lathe spindle-bearing system considering thermal effect is proposed to analysis the dynamic characteristics of system. The experimental results are in good agreement with the numerical simulation results, which verifies the correctness of the proposed model. The effects of spindle speed, pulley eccentricity and bearing preload on the dynamic behaviors of system are analyzed. In addition, the effects of rotational speed and preload on the contact angle, contact load and stiffness of bearings are also fully studied. Some conclusions are exhibited as follows:

The contact angle and contact load between balls and inner and outer raceways considering thermal effect are smaller than those without thermal effect. The bearing stiffness considering thermal effect is smaller than that without thermal effect. These are all attributed to the thermal deformation of bearing parts which makes the radial distance between the curvature centers of inner and outer raceways of bearing large and the temperature rise of bearing parts is uneven.

The response of system considering thermal effect is larger than the system without thermal effect, which is due to the decrease of bearing stiffness considering thermal effect.

In the whole range of rotational speed, the nonlinear characteristics of system considering thermal effect are richer than the system without considering thermal effect. Moreover, after the thermal effect is taken into account, the rotation speed of chaotic motion is advanced, and the interval of chaotic region is increased.

The rotational speed, pulley eccentricity and preload have great influence on the nonlinear characteristics of system which can be studied by means of time history curve, 3-D frequency spectrum curve, phase diagram, Poincare section and bifurcation diagram, among which pulley eccentricity and preload are the most sensitive to the influence of system.

Acknowledgements We would like to express our appreciation to Chinese National Natural Science Foundation (U1708254) and National Key R & D Program of China (2019YFB2004400) for supporting this research.

Data Availability The datasets generated during and analyzed during the current study are available from the corresponding author on reasonable request.

Declarations

Conflict of interest The author(s) declared no potential conflicts of interest with respect to the research, authorship, and/or publication of this article.

References

1. Zhao, H.T., Yang, J.G., Shen, J.H.: Simulation of thermal behavior of a CNC machine tool spindle. Int. J. Mach. Tools Manuf. **47**(6), 1003–1010 (2007). https://doi.org/10.1016/j.ijmachtools.2006.06.018
2. Xu, K.P., Wang, B., Zhao, Z.X., et al.: The influence of rolling bearing parameters on the nonlinear dynamic response and cutting stability of high-speed spindle systems. Mech. Syst. Signal PR. **136**, 131–136 (2020). https://doi.org/10.1016/j.ymssp.2019.106448
3. Than, V.T., Huang, J.H.: Nonlinear thermal effects on high-speed spindle bearings subjected to preload. Tribol. Int. **96**, 361–372 (2016)
4. Abele, E., Altintas, Y., Brecher, C.: Machine tool spindle units. CIRP Ann. Manuf. Technol. **59**, 781–802 (2010). https://doi.org/10.1016/j.cirp.2010.05.002
5. Mayr, J., Jedrzejewski, J., Uhlmann, E., et al.: Thermal issues in machine tools. CIRP Ann. Manuf. Technol. **61**, 771–791 (2012). https://doi.org/10.1016/j.cirp.2012.05.008
6. Xiang, S.T., Yao, X.D., Du, Z.C., Yang, J.G.: Dynamic linearization modeling approach for spindle thermal errors of machine tools. Mechatronics **53**, 215–228 (2018). https://doi.org/10.1016/j.mechatronics.2018.06.018
7. Yan, K., Hong, J., Zhang, J.H., et al.: Thermal-deformation coupling in thermal network for transient analysis of spindle-bearing system. Int. J. Therm. Sci. **104**, 1–12 (2016). https://doi.org/10.1016/j.ijthermalsci.2015.12.007
8. Zhang, Y.F., Li, X.H., Hong, J., et al.: Uneven heat generation and thermal performance of spindle bearings. Tribol. Int. **126**, 324–335 (2018). https://doi.org/10.1016/j.triboint.2018.04.035
9. Wu, W., Hu, J.B., Yuan, S.H., et al.: Numerical and experimental investigation of the stratified air-oil flow inside ball bearings. Int. J. Heat Mass Tran. **103**, 619–626 (2016)

10. Palmgren, A.: Ball and Roller Bearing Engineering, 3rd edn. Burbank Philadelphia, USA (1959)
11. Harris, T.A., Kotzalas, M.N.: Rolling bearing analysis: advanced concepts of bearing technology, 5th edn. CRC Press, Boca Raton (2006)
12. Brecher, C., Hassis, A., Rossaint, J.: Cage friction in high-speed spindle bearings. Tribol. Int. **57**, 77–85 (2014)
13. Than, V.T., Wang, C.C., Ngo, T.T., et al.: Estimating time-varying heat sources in a high speed spindle based on two measurement temperatures. Int. J. Therm. Sci. **111**, 50–65 (2017)
14. Tong, V.C., Hong, S.W.: Study on the running torque of angular contact ball bearings subjected to angular misalignment. P. I. Mech. Eng. J-J. Eng. **232**, 890–909 (2018)
15. Oktaviana, L., Van-Canh, T., Hong, S.W.: Skidding analysis of angular contact ball bearing subjected to radial load and angular misalignment. J. Mech. Sci. Technol. **33**, 837–845 (2019)
16. Zhang, X., Xu, H., Chang, W., et al.: Torque variations of ball bearings based on dynamic model with geometrical imperfections and operating conditions. Tribol. Int. **133**, 193–205 (2019)
17. Pouly, F., Changenet, C., Ville, F.: Investigations on the power losses and thermal behavior of rolling element bearings. PIMechEngJ-JEng. **224**, 925–933 (2010)
18. Jafar, T., Khonsari, M.M.: Experimental testing and thermal analysis of ball bearings. Tribol. Int. **60**, 93–103 (2013). https://doi.org/10.1016/j.triboint.2012.10.009
19. Lin, C.W., Tu, J.F., Kamman, J.: An integrated thermal-mechanical-dynamic model to characterize motorized machine tool spindles during very high speed rotation. Int. J. Mach. Tool Manuf. **43**, 1035–1050 (2003). https://doi.org/10.1016/S0890-6955(03)00091-9
20. Mohammed, A., Omar, S.M.: Analytical study of thermal variation impact on dynamics of a spindle bearing system. Proc. Inst Mech. Eng. Part K: J Multi-body Dyn. (2019). https://doi.org/10.1177/1464419319841687
21. Zheng, D.X., Chen, W.F., Li, M.M.: An optimized thermal network model to estimate thermal performances on a pair of angular contact ball bearings under oil-air lubrication. Appl. Therm. Eng. **131**, 328–339 (2018). https://doi.org/10.1016/j.applthermaleng.2017.12.019
22. Zheng, D.X., Chen, W.F.: Thermal performances on angular contact ball bearing of high-speed spindle considering structural constraints under oil-air lubrication. Tribol. Int. **109**, 593–601 (2017). https://doi.org/10.1016/j.triboint.2017.01.035
23. Zheng, D.X., Chen, W.F.: Effect of structure and assembly constraints on temperature of high-speed angular contact ball bearings with thermal network method. Mech. Syst. Signal PR. (2020). https://doi.org/10.1016/j.ymssp.2020.106929
24. Liu, J.L., Ma, C., Wang, S.L., et al.: Thermal-structure interaction characteristics of a high-speed spindle-bearing system. Int. J. Mach. Tool Manuf. **137**, 42–57 (2021)
25. Ertürk, A., Özgüven, H.N., Budak, E.: Analytical modeling of spindle-tool dynamics on machine tools using Timoshenko beam model and receptance coupling for the prediction of tool point FRF. Int. J. Mach. Tool Manuf. **46**, 1901–1912 (2006). https://doi.org/10.1016/j.ijmachtools.2006.01.032
26. Bai, C., Zhang, H., Xu, Q.: Subharmonic resonance of a symmetric ball bearing-rotor system. Int. J. Non-linear Mech. **50**, 1–10 (2013). https://doi.org/10.1016/j.ijnonlinmec.2012.11.002
27. Sinou, J.-J.: Non-linear dynamics and contacts of an unbalanced flexible rotor supported on ballbearings. Mech. Mach. Theory. **44**, 1713–1732 (2009). https://doi.org/10.1016/j.mechmachtheory.2009.02.004
28. Han, Q., Chu, F.: Parametric instability of flexible rotor-bearing system under time-periodic base angular motions. Appl. Math. Model. **39**, 4511–4522 (2015). https://doi.org/10.1016/j.apm.2014.10.064
29. Li, Y.S., Chen, X.A., Zhang, P.: Dynamics modeling and modal experimental study of high speed motorized spindle. J. Mech. Sci. Technol. **31**(3), 1049–1056 (2017). https://doi.org/10.1007/s12206-017-0203-4
30. Xi, S.T., Cao, H.R., Chen, X.F.: A dynamic modeling approach for spindle bearing system supported by both angular contact ball Bearing and floating displacement bearing. J. Manuf. Sci. E-T ASME. (2018). https://doi.org/10.1115/1.4038687
31. Li, H., Shin, Y.C.: Integrated dynamic thermo-mechanical modeling of high speed spindles, Part 1: Model Development. J Manuf Sci E-T ASME. **126**, 148–158 (2004). https://doi.org/10.1115/1.1644545
32. Li, H., Shin, Y.C.: Analysis of bearing configuration effects on high speed spindles using an integrated dynamic thermo-mechanical spindle model. Int. J. Mach. Tool Manuf. **44**, 347–364 (2004). https://doi.org/10.1016/j.ijmachtools.2003.10.011
33. Truong, D.S., Kim, B.S., Ro, S.K.: An analysis of a thermally affected high-speed spindle with angular contact ball bearings. Tribol. Int. (2021). https://doi.org/10.1016/j.triboint.2021.106881
34. Zheng, D.X., Chen, W.F., Zheng, D.T.: An enhanced estimation on heat generation of angular contact ball bearings with vibration effect. Int. J. Therm. Sci. (2021). https://doi.org/10.1016/j.ijthermalsci.2020.106610
35. Liu, J.L., Ma, C., Gui, H.Q., Wang, L.: Thermally-inducederrorcompensationofspindlesystembasedonlong-shorttermmemoryneuralnetworks. Appl. Soft Comput. (2021). https://doi.org/10.1016/j.asoc.2021.107094
36. Cao, Y., Alyintas, Y.: A general method for the modeling of spindle-bearing systems. J. Mech. Design. **126**, 557–566 (2004). https://doi.org/10.1115/1.1802311
37. Jones, A.B.: A general theory for elastically constrained ball and radial roller bearings under arbitrary load and speed conditions. ASME J. Basic Eng. **82**, 309–320 (1960). https://doi.org/10.1016/j.ijmachtools.2006.08.006
38. Muzychka, Y., Yovanovitch, M.: Thermal resistance of model for non circular moving heat sourceson a half space. J. Heat Transf. **123**, 624–632 (2001). https://doi.org/10.1115/1.1370516
39. Salerno, L.J., Kittel, P.: Thermal conductance of augmented pressed metallic contacts at liquid heliu temperatures. Cryogenics (1993). https://doi.org/10.1016/0011-2275(93)90002-6
40. Mohammadpour, M., Johns-Rahnejat, P.M., Rahenjat, H.: Roller bearing dynamics under transient thermal-mixed

non-Newtonian elastohydrodynamic regime of lubrication. P I Mech. Eng. K-J Mul. **229**, 407–423 (2015). https://doi.org/10.1177/1464419315569621
41. Latif, M.J.: Heat convection, 2nd edn. Springer-Verlag, Berlin (2009)
42. Holman, J.P.: Heat Transfer, 7th edn. McGraw-Hill, New York (1989)
43. Bjorklund, I.S., Kays, W.M.: Heat transfer between concentric rotating cylinders. Trans. ASME **81**, 175–186 (1959). https://doi.org/10.1115/1.4008173
44. Wagner, C.: Heat transfer from a rotating disk in ambient air. J. Appl. Phys. **19**, 837–839 (1948). https://doi.org/10.1063/1.1698216
45. Churchill, S.W., Chu, H.H.S.: Correlation equations for laminar and turbulent free convection from a vertical plate. Int. J. Heat Mass Transf. **18**, 1323–1329 (1975). https://doi.org/10.1016/0017-9310(75)90222-7
46. Stein, J.L., Tu, J.F.: A state-space model for monitoring thermally induced preload in anti-friction spindle bearings of high-speed machine tools. J. Dyn. Syst. Meas. Control. **116**, 372–386 (1994). https://doi.org/10.1115/1.2899232
47. Timoshenko, S., Goodier, J.N.: Theory of elasticity, 3rd edn. McGraw-Hill, New York (1969)
48. Zhang, X.N., Han, Q.K., Peng, Z.K., Chu, F.L.: A new nonlinear dynamic model of the rotor-bearing system considering preload and varying contact angle of the bearing. Commun. Nonlinear Sci. **22**, 821–841 (2015). https://doi.org/10.1016/j.cnsns.2014.07.024
49. Gan, C.B., Wang, Y.H., Yang, S.X., et al.: Nonparametric modeling and vibration analysis of uncertain Jeffcott rotor with disc offset. Int. J. Mech. Sci. **78**, 126–134 (2014). https://doi.org/10.1016/j.ijmecsci.2013.11.009
50. Chandra, N.H., Sekhar, A.S.: Swept sine testing of rotor-bearing system for damping estimation. J. Sound Vib. **333**, 604–620 (2014). https://doi.org/10.1016/j.jsv.2013.09.009